Glimmers in the Cosmic Dawn. III. On the Photometrically Determined Black Hole Mass to Stellar Mass Relation across Cosmic Time

The Astrophysical Journal, 999:175 (22pp), 2026 March 10 https://doi.org/10.3847/1538-4357/ae3d04

Glimmers in the Cosmic Dawn. III. On the Photometrically Determined Black Hole Mass to Stellar Mass Relation across Cosmic Time*

Alice R. Young[1], Matthew J. Hayes[1], Alberto Saldana-Lopez[1], Axel Runnholm[1], Vieri Cammelli[2], Jonathan C. Tan[3,4], Richard S. Ellis[5], Benjamin W. Keller[6], Jens Melinder[1], and Jasbir Singh[7]
[1] Stockholm University, Department of Astronomy and Oskar Klein Centre for Cosmoparticle Physics, AlbaNova University Centre, SE-10691 Stockholm, Sweden; alice.young@astro.su.se
[2] Department of Physics, Informatics & Mathematics, University of Modena & Reggio Emilia, via G. Campi 213/A, 41125, Modena, Italy
[3] Department of Space, Earth & Environment, Chalmers University of Technology, SE-412 96 Gothenburg, Sweden
[4] Department of Astronomy, University of Virginia, Charlottesville, VA 22904, USA
[5] Department of Physics and Astronomy, University College London, Gower Street, London WC1E 6BT, UK
[6] Department of Physics and Materials Science, University of Memphis, 3720 Alumni Avenue, Memphis, TN 38152, USA
[7] INAF—Astronomical Observatory of Brera, via Brera 28, I-20121 Milan, Italy
Received 2025 August 21; revised 2026 January 20; accepted 2026 January 21; published 2026 March 2

Abstract

We present the results from performing spectral energy distribution (SED) fitting on 121 variable active galactic nuclei (AGN) candidates in the Hubble Ultra Deep Field using photometry from both the Hubble Space Telescope and the James Webb Space Telescope (JWST) covering 0.2–4.8 μm. We designed a bespoke SED fitting code, which decomposes the total SED into its stellar and AGN contributions. Our SED fitting retrieves a significant contribution to the total SED from an AGN template for 26 of our variable sources with $0 < z < 7$. We leverage the model AGN spectrum to estimate black hole masses ($M_{\rm BH}$) using the measured luminosity at 5100 Å and local empirical calibrations. Common with recently discovered JWST broad-line AGN, we observe a trend in the $M_{\rm BH}$–M_* plane where low-redshift sources have $M_{\rm BH}$ that agrees with local relations while high-redshift sources have increasingly overmassive black holes with respect to the stellar mass (M_*) of their host galaxies. Within our sample, we identify two IMBH candidates hosted by dwarf galaxies at $z < 1$ featuring overmassive black holes in the $M_{\rm BH}$–M_* plane, similarly to our high-redshift sources. Finally, our SED fitter successfully retrieves the AGN nature of one source at $z > 6$. This object has $z_{\rm phot} = 6.74$, and we estimate a lower limit on its black hole mass of $\log_{10}(M_{\rm BH}/M_\odot) > 7.36$.

Unified Astronomy Thesaurus concepts: High-redshift galaxies (734); Active galactic nuclei (16); Galaxy evolution (594)

1. Introduction

Despite evidence that supermassive black holes (SMBHs) can be found in the nuclei of most massive galaxies in the local Universe, the physical mechanisms that lead to the tight correlations between SMBH mass and the bulge properties of their host galaxies remain uncertain (J. Kormendy & L. C. Ho 2013; J. E. Greene et al. 2020). Theories backed by cosmological simulations suggest that the coevolutionary growth may be the result of galaxy and black hole (BH) mergers as well as the feedback of accreting BHs called active galactic nuclei (AGN), which can regulate the accumulation of stellar mass within a galaxy (G. L. Granato et al. 2004; P. F. Hopkins et al. 2006; Y. Li et al. 2007; D. Sijacki et al. 2009; M. Volonteri 2010; R. Valiante et al. 2016; J. E. Greene et al. 2020; K. Inayoshi et al. 2020; X. Fan et al. 2023; S. Koudmani et al. 2022; A. Trinca et al. 2022; J. S. Bennett et al. 2024; M. Volonteri et al. 2023). In order to better constrain theoretical predictions for the coevolutionary nature of SMBH and galaxy relations, it is essential to probe the SMBH population beyond the local volume and into the high-redshift (high-z) Universe.

Before the advent of the James Webb Space Telescope (JWST), observations of SMBHs beyond $z \sim 4$ were difficult to achieve. This was due to the fact that relevant diagnostic lines were redshifted beyond the wavelength constraints of the available detectors as well as the lack of sensitivity to faint, less massive galaxies and SMBHs at higher redshift. As such, it was primarily only possible to detect the most luminous AGN, namely, quasars at $z \gtrsim 4$ (e.g., S. J. Warren et al. 1987; D. P. Schneider et al. 1994; I. M. Hook & R. G. McMahon 1998; X. Fan et al. 1999; D. P. Schneider et al. 2000; X. Fan et al. 2001). With the discovery of quasars at $z > 7$, it was found that these objects had masses exceeding several billions of solar masses already within the first few billions of years after the Big Bang (D. J. Mortlock et al. 2011; E. Bañados et al. 2017; Y. Matsuoka et al. 2018, 2019; F. Wang et al. 2018; J. Yang et al. 2019, 2020; X. Fan et al. 2023). This was in contention with many simulations that struggled to grow SMBHs sufficiently to achieve such large SMBH masses at these redshifts (J. McCaffrey et al. 2025). This result has been

* This research is based on observations made with the NASA/ESA Hubble Space Telescope obtained from the Space Telescope Science Institute, which is operated by the Association of Universities for Research in Astronomy, Inc., under NASA contract NAS 5-26555. These observations are associated with GO programs 1563, 12498, 17073. This work is also based on observations made with the NASA/ESA/CSA James Webb Space Telescope. The data were obtained from the Mikulski Archive for Space Telescopes at the Space Telescope Science Institute, which is operated by the Association of Universities for Research in Astronomy, Inc., under NASA contract NAS 5-03127 for JWST. These observations are associated with GTO programs 1180, 1181, 1210, 1286 and GO programs 1895, 1963, 3215.

exacerbated by recent discoveries with JWST, which have identified overmassive BHs at high-z, either necessitating extreme growth rates or favoring a heavy seeding scenario in the early Universe to explain the observed masses at these early cosmological times (Y. Harikane et al. 2023; V. Kokorev et al. 2023; R. L. Larson et al. 2023; H. Übler et al. 2023; L. J. Furtak et al. 2024; R. Tripodi et al. 2025; R. Maiolino et al. 2024a; H. B. Akins et al. 2025; R. P. Naidu et al. 2025; A. J. Taylor et al. 2025; J. Zhang et al. 2025).

A variety of SMBH seeding scenarios have been invoked to attempt to resolve this observational disparity with theoretical predictions (J. E. Greene et al. 2020; K. Inayoshi et al. 2020; J. Regan & M. Volonteri 2024), including direct collapse BHs (M. G. Haehnelt & M. J. Rees 1993; V. Bromm & A. Loeb 2003; M. C. Begelman et al. 2006; S. Chon et al. 2016; J. H. Wise et al. 2019), stellar mergers in dense star clusters (M. Freitag et al. 2006; D. P. Schneider et al. 2023), super-Eddington growth of Population III (Pop III) stars (P. Madau & M. J. Rees 2001; A. Trinca et al. 2022), and unique processes of the very first generation of Pop III stars (designated Pop III.1; C. F. McKee & J. C. Tan 2008), which allow these stars to leave behind supermassive remnants that act as SMBH seeds with masses $\sim 10^5 M_\odot$ (C. F. McKee & J. C. Tan 2008; N. Banik et al. 2019; J. Singh et al. 2023; V. Cammelli et al. 2025; M. Sanati et al. 2025). Degeneracies that exist in the predictions of these seeding theories can be constrained by probing the population of SMBHs at high redshift ($z > 6$) highlighting the importance of observations that target the detection of faint, lower-mass, and more distant AGN.

A multitude of methods exist for the detection of these objects including X-ray detections with luminosities exceeding those produced by stellar populations (SPs), the detection of emission lines with ionization energies greater than the typical output of stars, as well as the previously mentioned characteristic broadened emission lines that designate a broad-line AGN (BL-AGN). An additional observational tool comes from using photometric variability to detect variations in brightness within the nucleus of a host galaxy, which can be explained by changes in the accretion rate of a central SMBH. By using multiple images of approximately equal depth, it is possible to test an entire field for variability without any need for observational preselection unlike slit-based spectroscopic methods. Photometric variability also allows for a more complete sample of luminosities to be tested for the presence of AGN in comparison to other methods where typically only the brightest candidates are flagged for spectroscopic follow-up. The ability photometric variability offers to probe fainter luminosities also allows for lower-mass BHs to be probed at each redshift. Leveraging photometric variability has been successful at identifying AGN at intermediate redshifts using deep images taken with the Hubble Space Telescope (HST; S. H. Cohen et al. 2006; E. Pouliasis et al. 2019; R. O'Brien et al. 2024). With longer baselines in time, variability with HST has even successfully probed AGN candidates out to $6 < z < 8$ (M. J. Hayes et al. 2024; V. Cammelli et al. 2025). Such a census of variable SMBHs can offer strong constraints for simulations predicting SMBH seeding in the early Universe via the observed comoving number density (M. J. Rees 1978; M. Volonteri 2010; N. Banik et al. 2019; K. Inayoshi et al. 2020; J. Singh et al. 2023). In addition, the observational power of variability studies is fortified by the addition of legacy data across a wide range of wavelengths, which can then be used to disentangle the AGN contribution to the total flux by modeling the spectral energy distributions (SEDs) of these sources through SED fitting.

In this paper, we present a bespoke SED fitting code we have developed utilizing the semiempirical AGN templates presented in M. J. Temple et al. (2021) in combination with SP models from G. Bruzual & S. Charlot (2003). We use this SED fitting tool to determine physical properties of the central SMBH and its host galaxy. We achieve this using spectral decomposition in order to understand the underlying contributions of both an SP and an AGN to the total SED of our variable sources. This decomposition method is inspired by recent works seeking to determine the nature of the mysterious population of compact objects at $z > 3$ featuring characteristic "v-shaped" SEDs (G. Barro et al. 2024; D. D. Kocevski et al. 2023; I. Labbe et al. 2024) and often broad Balmer emission lines termed "little red dots" (LRDs; L. J. Furtak et al. 2023; D. D. Kocevski et al. 2023; J. E. Greene et al. 2024; V. Kokorev et al. 2024; J. Matthee et al. 2024; B. Wang et al. 2025). A popular method includes modeling the SEDs of these objects to understand if they are better represented by a pure stellar component or if an AGN is necessary (for examples, see H. B. Akins et al. 2025; G. C. K. Leung et al. 2025; D. J. Setton et al. 2025; Y. Ma et al. 2025; B. Wang et al. 2025). However, we note that the goal of this work is not identical to those studying the nature of LRDs. Namely, since we have already identified our sources as variable AGN, we are not trying to ascertain whether an AGN is present in our sources (as in the LRD scenario); we are instead seeking to determine if our SED fitter can successfully recover the AGN nature of our sources.

Our sample consists of 121 sources in the Hubble UltraDeep Field (HUDF) with $z = 0$–8 detected with variability measured at the 2.5σ level in V. Cammelli et al. (2025). From this sample of variable SMBH candidates, we aim to determine what fraction of our sources can be retrieved as AGN via SED fitting as well as physical properties of our variable sources. In particular, we seek to determine the BH masses ($M_{\rm BH}$) for a subset of variable BHs and identify how these evolve with respect to the stellar mass of the host galaxies for the range of redshifts represented by our sample. Our SED modeling is performed on point-spread function (PSF)-matched photometry from 26 HST+JWST filters covering a wavelength range from 0.2 to 4.8 μm using only seven free parameters. Our SED fits provide estimates for the stellar mass (M_*) as well as a model AGN spectrum, which we use to determine the luminosity of the AGN at 5100 Å (L_{5100}). This, in combination with the relation from S. Kaspi et al. (2000), allows us to estimate $M_{\rm BH}$.

Additionally, this work offers a unique opportunity to compare the trends seen in the $M_{\rm BH}$–M_* plane using an alternative method to calculate $M_{\rm BH}$ from those typically employed for the recently discovered high-redshift BL-AGN with JWST.

This paper is structured as follows: Section 2 details the HUDF imaging campaign and the data reduction processes used to achieve approximately equal depths in both epochs of each filter pair used for variability detection. Additionally, we detail the PSF matching executed to produce the photometry used in our SED fitting. Section 3 details the creation of our bespoke SED fitting tool and the methods we employ to select

either a pure SP SED or a combined stellar and AGN model. Section 4 details how we retrieve AGN contributions for our variable sources using SED fitting as well as how we estimate the BH masses for a subset of our variable sources. Finally, in Section 5, we discuss our estimated BH masses and their evolution with redshift as well as the various factors that could affect our estimates. These include SED reddening and the impact of variability on our SED fits. We also present two dwarf galaxies hosting intermediate mass black hole (IMBH) candidates and discuss the $M_{\rm BH}$ calculated for our highest-redshift source and what this estimate implies about BH seeding.

Throughout this work, we use the AB magnitude system (J. B. Oke & J. E. Gunn 1983) and assume a flat ΛCDM cosmology with $H_0 = 70\,{\rm km\,s^{-1}\,Mpc^{-1}}$, $\Omega_m = 0.3$, and $\Omega_\Lambda = 0.7$.

2. Observations and Data Reduction

2.1. Processing WFC3/IR Epochs for Variable Detection

In order to detect our variable sources, two sets of images corresponding to two epochs of observation were analyzed for each of the F105W, F140W, and F160W WFC3/IR filters. The data were originally presented in M. J. Hayes et al. (2024); however, a more detailed description of the reduction procedure is provided here. The HUDF was originally imaged with F105W, F125W, and F160W in 2008–2009 (GO 11563, UDF09; PI: Illingworth) followed by repeated imaging in 2012 with F105W, F140W, and F160W (GO 12498, UDF12; PI: Ellis). Finally, in 2023, the HUDF was imaged a third time with F140W to match the depth of the UDF12 campaign (GO 17073; PI: Hayes). This longer baseline in time of ∼11 yr is particularly well suited to probing the variability of AGN at high-z in order to overcome the large cosmological time dilation factor.

We performed independent reductions of the 2009 and 2012 epochs for the F105W and F160W filters as well as a rereduction of the F140W 2012 image. Additionally, we utilize the High Level Science Products (HLSPs) from the Mikulski Archive for Space Telescopes (MAST) as reference images and compare the depth of our rereductions to the original HLSPs. The reduction procedure was slightly altered between the F105W and F140W/F160W images as additional care is required to correct for the time-varying background resulting from helium line emission being captured by the detector with the F105W filter when HST leaves Earth's shadow (see G. Brammer 2016). Therefore, for the F105W epochs, we apply an additional correction to "flatten the ramp" of the charge accumulation history before further processing.

For F105W, the data are processed using the `calwf3` pipeline up to the cosmic-ray identification step. The ramp is then flattened before being fed back into `calwf3` pipeline to complete the cosmic-ray identification and result in the final reduced files as described in G. Brammer (2016). For F140W and F160W images, this step was not applied, and all reduced files were retrieved from MAST having already been processed with the `calwf3` pipeline.

The final calibrated images in each association output from the pipeline require additional processing, namely, satellite trail identification and persistence correction. For the 2009 and 2012 epochs, persistence is corrected using persistence maps from the PERSIST Search STScI Archive to identify the affected pixels in the quality flags of each file so that these pixels are masked during the combination process. For the 2023 data, these persistence masks are created by eye to flag areas of strong persistence effects. Further, for all epochs, satellite trails are flagged in a similar manner, after being identified with the WfcWrapper for the `TrailFinder` tool within STScI's ACSTOOLS Python package (P. L. Lim et al. 2020).

After these corrections, the images in each association are combined using `AstroDrizzle` (STSCI Development Team 2012). The relevant HLSP is used as the reference for the World Coordinate System (WCS), rotation, and pixel scale, which is drizzled to be $0\farcs06\,{\rm pixel^{-1}}$. To be consistent with values used by A. M. Koekemoer et al. (2013) in the UDF12 data products, the pixfrac, $p = 0.8$. The scale, $s = 6/13$, arises from the WFCIR native pixel scale of $0\farcs13$ pixel^{-1} and the drizzled pixel scale of $0\farcs06$ pixel^{-1} used in the HLSP data product. `TweakReg` is then used to refine the WCS, again, using the HLSP as a reference. Finally, for consistency with A. M. Koekemoer et al. (2013), the images have a best-fit 2D median background subtracted to remove residual structures seen in the exposures before being drizzled together using `combine_type = "median"` to create the final image at each epoch.

2.2. PSF-matched Photometry

The images for which we perform the photometry used as the input for our SED analysis come from several programs. In addition to the Wide Field Camera 3 (WFC3)/IR filter images we reprocessed, the HLSP for the F125W filter (PI: Illingworth) is also used in the analysis. We also employ HLSPs from the Hubble Ultraviolet Ultra Deep Field (UVUDF; PI: Teplitz; H. I. Teplitz et al. 2013; M. Rafelski et al. 2015) in the WFC3/UVIS F225W, F275W, and F336W filters obtained from the MAST. Additionally, HST images in the Advanced Camera for Surveys (ACS)/WFC F435W, F606W, F775W, F814W, and F850LP filters are from the Hubble eXtreme Deep Field (XDF), which combines observations taken from 2002 July to 2012 December from 19 different HST programs (G. D. Illingworth et al. 2013). We also include JWST HLSPs from the JWST Advanced Deep Extragalactic Survey (JADES; PI: Eisenstein & Luetzgendorf; D. J. Eisenstein et al. 2025; M. J. Rieke et al. 2023b) and the JWST Extragalactic Medium-band Survey (JEMS; PI: Williams, Tacchella & Maseda C. C. Williams et al. 2023) in 14 filters covering the GOODS-S field, which contains the HUDF footprint (F090W, F115W, F150W, F182M, F200W, F210M, F277W, F335M, F356W, F410M, F430M, F444W, F460M, and F480M).

Before performing PSF matching, we aligned the HST images to the GAIA coordinates using `TweakReg`. We also matched the pixel scale of the NIRCam images to the drizzled HST pixel scale of $0\farcs06$ pixel^{-1} and cropped the NIRCam images to have the same pixel dimensions as the HUDF images using `SWarp` (E. Bertin et al. 2002). Some residual pixel grid/WCS alignment offsets were resolved using Astropy's `reproject_exact` function (T. Robitaille et al. 2020).

With the images all aligned to the same pixel grid, we then performed the PSF matching. PSFs were obtained from STScI's instrumentation archive for the WFC3/IR and UVIS filters, while the ACS PSFs were generated from the STScI ACS/WFC Focus-Diverse ePSF generator. Finally, NIRCam

PSFs were generated using STPSF (M. D. Perrin et al. 2012). All PSFs were matched to the F480M PSF using a matching kernel generated with PyPHER (A. Boucaud et al. 2016). PyPHER applies Wiener filtering (N. Wiener 1949) to generate PSF-matched kernels with an adjustable regularization parameter, which we set to $r = 0.003$ to reduce high-frequency noise in the kernels (J. R. Weaver et al. 2024). As discussed in J. R. Weaver et al. (2024), PyPHER is capable of producing reliable matching kernels without the need to select a window function as would be required by Photutils, thereby offering a more stable kernel solution over all of the filter PSFs used in this study. The matching kernels were then convolved to the relevant filter using the convolve tool from Astropy's convolution package (Astropy Collaboration et al. 2013, 2018, 2022). An exception is applied to the UVIS filters for which the matching kernels produced significant convolution artifacts in the final convolved images. This is likely due to the fact that the UVIS PSFs are significantly smaller than the F480M NIRCam PSF, and, as such, for the UVIS filters, the images were simply convolved using the F480M PSF directly to reduce the effects of convolution artifacts in the UVIS images. This is an appropriate approximation given that the UVIS PSFs are on the order of ∼20 times narrower, meaning the true matching kernel will be very close to the F480M PSF.

2.3. Defining a Photometric Catalog

A deep WFC3/IR image was created using all six of the reprocessed F105W, F140W, and F160W images as well as the F125W HLSP image. This ultradeep image was used as the detection image in Source Extractor (E. Bertin & S. Arnouts 1996) to produce a reference detection catalog containing all of the sources in HUDF. We then iteratively performed aperture photometry on all 29 filter images using an aperture diameter of 4 pixels (corresponding to $\sim 0\farcs24$). This aperture was chosen to be about twice the full width at half-maximum (FWHM) of the F480M PSF, and its size is optimized to capture the bulk of the light from compact sources. It is plausible that some stellar light may be missing from large extended galaxies at very low redshifts, but visual inspection of our variable sources invariably shows this to be negligible. The final photometry is then converted to universal physical units of mJy for all filters. The measured fluxes for our sources were crossmatched to sources in the JADES photometric catalog (D. J. Eisenstein et al. 2025) and were found to be in good agreement for all of the available NIRCam filters.

Finally, we corrected for the underestimated errors reported by Source Extractor. For this, we normalized the F480M PSF to an injection magnitude and iteratively inserted 10 of these PSFs into each PSF-matched filter image 100 times to reach a total of 1000 injected sources in each image at each injected magnitude. For most filters, this range of magnitudes was between 26.0 and 31.5; however, UVIS filters required a wider range from 25 to 31.5 mag to determine the 90% completeness limit for each image. The completeness curves for each filter are shown in Figure 1; and a summary of the images and their limiting magnitudes is presented in Table 1. The standard deviation for the distribution of retrieved source magnitudes was compared to Source Extractor magnitude errors determined for the HUDF sources in our reference detection catalog. This comparison was then used to determine a correction factor, which could be applied to the photometric errors of our sources as a function of source magnitude for each filter. A minimum error of 5% was defined after the error correction was applied to account for the absolute calibration uncertainties of the telescopes and minor uncertainties resulting from the PSF matching. For a more detailed discussion of the error correction applied, see Appendix A.

Our final sample of sources for which we perform SED fitting consists of the 121 sources with variability detected at the 2.5σ level reported in V. Cammelli et al. (2025). For each source in the sample, we also check that the photometry does not contain any pixels that are masked in a given filter (i.e., due to gaps in mosaic images for JADES and JEMS images) using the segmentation maps generated by Source Extractor while defining our reference detection catalog. Finally, fluxes that are measured to be below the 90% completeness limit of a given filter are designated as upper limits, and the value is set to half the limiting magnitude converted to mJy with corresponding errors of the same value as suggested as one of the recommended options for CIGALE (M. Boquien et al. 2019).

3. Modeling

In order to learn more about the physical properties of our variable sources, we designed a bespoke SED fitting code, which decomposes the contribution of an SP from the host galaxy along with an AGN component to model our 26 band photometry covering ultraviolet (UV) to infrared wavelengths. We apply a cut to the sample from V. Cammelli et al. (2025), which stipulates that we only perform SED fitting on sources that have a signal-to-noise ratio (S/N) > 5 in at least eight filters. This equates to the maximal number of free parameters in our SED fitting code (when we use the combined AGN + stellar model) plus one in order to be confident that our photometry is sufficient to properly constrain our SED model. Of the 26 available filters, the S/N condition can be met by any 8 filters to avoid limiting the wavelength coverage to only shorter or longer wavelengths. After removing sources that do not meet this requirement, only four objects have fewer than 26 filters with detections below the S/N < 5 threshold (also excluding filters where only upper limits are measured) with the lowest number of detections being 20 for object 56. Even this source has detections covering nearly the full wavelength range from 0.4 to 4.4 μm. Therefore, all of our sources have sufficient photometry to produce reliable fits.

Our motivation to develop a new SED fitting code derived from numerous tests showing that using the SKIRTOR model implemented in other SED fitting codes (i.e., CIGALE) did not provide good fits for many of our variable sources. In particular, it was not possible to achieve fluxes representative of the photometry observed in our redder wavelength NIRCam filters using the SKIRTOR model without significantly underpredicting the fluxes at bluer wavelengths. Even when tuned to be as blue as possible, the SKIRTOR model was unsuccessful at replicating the flux at wavelengths that include the WFC3/IR filters. Since these are the filters where the variability of our objects is detected, we would, therefore, expect to see a significant contribution to the flux from an AGN template at those wavelengths. We observed this effect in a number of sources for which the AGN classification is well supported. One such case includes a variable source at $z = 1.95$, which was originally presented in M. J. Hayes et al. (2024) as source

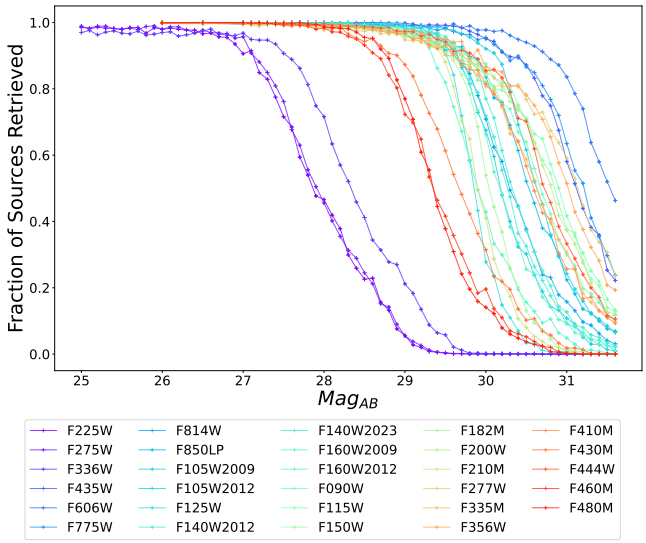

Figure 1. Completeness curves for each PSF-matched filter. These are tabulated by injecting each image with point sources modeled by the F480M PSF iteratively normalized to a given injection magnitude and determining the number of injected sources retrieved by `Source Extractor`. The limiting magnitude of each filter is then set to the injected magnitude in the bin preceding the bin where the number retrieved is below 90%.

1051264. For this source, the difference images show a pointlike variable component in the nucleus of an elongated disk, strongly indicating the presence of an AGN. Despite this evidence, when fit with CIGALE, this source consistently came back with a 0% AGN fraction, meaning the AGN contributed no flux to the total IR luminosity of the CIGALE fits. Upon further investigation, it was clear that the `SKIRTOR` model could not be parameterized in an appropriate way to capture the photometry of this source and several others featuring a similarly blue SED. Whether or not this source necessarily came back with a significant AGN contribution was not a significant concern, but the fact that there was no way for the `SKIRTOR` model to match our photometry indicated the need for a different set of AGN templates. A desire to use an AGN model that provided better fits to our photometry prompted our development of a new SED fitting algorithm, which we detail below.

3.1. Stellar Population Model

The stellar spectra for our SED fitter are generated using the Bayesian Analysis of Galaxies for Physical Inference and Parameter EStimation (BAGPIPES) code (A. C. Carnall et al. 2018). BAGPIPES uses the updated G. Bruzual & S. Charlot (2003) SP synthesis templates with a P. Kroupa (2001) stellar initial mass function (IMF), including the MILES stellar spectral library (J. Falcón-Barroso et al. 2011) and the stellar evolutionary tracks of A. Bressan et al. (2012) and P. Marigo et al. (2013). Nebular continuum and emission lines were added by processing the stellar emission through the CLOUDY v17.00 photoionization code (G. J. Ferland et al. 2017). We created a multidimensional grid of SED models by adopting a parametric star formation history (SFH) following a delayed-τ prescription, where the star formation rate (SFR) changes as a function of time as $\mathrm{SFR}(t) = te^{-t/\tau}$. We sample a hundred logarithmically spaced bins for the stellar age, t (between 1 Myr and 10 Gyr), as well as 10 bins for the e-folding time, τ, designed to have increased sampling for low values of τ starting with a minimum timescale of 2 Myr. All these parameters are summarized in Table 2.

The metallicity is assumed to be the same for the stars and the gas, with possible values of 0.05, 0.1, 0.2, 0.5, 1, and 2 $Z_{\odot}$, where $Z_{\odot} = 0.02$. All models formed a total mass of $10^6 M_{\odot}$, and assume a fixed ionization parameter for the nebular emission of $\log U = -2.5$. The resulting SEDs were then linearly interpolated within the grid using the `RegularGridInterpolator` function, from the SciPy (P. Virtanen et al. 2020) package.

Table 1
Summary of Filter Images Used for PSF-matched Photometry

Filter	$\mathrm{Mag_{AB,Lim}}$	Program ID	PI Name	HLSP Program
F225W	27.1	12534	Teplitz	UVUDF
F275W	27.1	12534	Teplitz	UVUDF
F336W	27.5	12534	Teplitz	UVUDF
F435W	30.2	Numerous[a]	Numerous[a]	XDF
F606W	30.7	Numerous[a]	Numerous[a]	XDF
F775W	30.2	Numerous[a]	Numerous[a]	XDF
F814W	29.6	Numerous[a]	Numerous[a]	XDF
F850LP	29.7	Numerous[a]	Numerous[a]	XDF
$\mathrm{F105W_{2009}}$	29.6	11563	Illingworth	HUDF09
$\mathrm{F105W_{2012}}$	30.1	12498	Ellis	HUDF12
F125W	29.5	11563	Illingworth	HUDF09
$\mathrm{F140W_{2012}}$	29.7	12498	Ellis	HUDF12
$\mathrm{F140W_{2023}}$	29.7	17073	Hayes	HUDF23
$\mathrm{F160W_{2009}}$	29.6	11563	Illingworth	HUDF09
$\mathrm{F160W_{2012}}$	29.3	12498	Ellis	HUDF12
F090W	29.5	1180	Eisenstein	JADES
F115W	29.7	1180	Eisenstein	JADES
F150W	29.5	1180	Eisenstein	JADES
F182M	29.5	1895	Oesch	JADES
F200W	29.7	1180	Eisenstein	JADES
F210M	29.4	1895	Oesch	JADES
F277W	29.7	1180	Eisenstein	JADES
F335M	29.6	1180	Eisenstein	JADES
F356W	29.7	1180	Eisenstein	JADES
F410M	29.6	1180	Eisenstein	JADES
F430M	28.9	1963	Williams	JADES
F444W	29.8	1180	Eisenstein	JADES
F460M	28.6	1963	Williams	JADES
F480M	28.7	1963	Williams	JADES

Notes. This includes the limiting magnitudes of each image ($\mathrm{Mag_{AB,\,Lim}}$) calculated from the source injections described in Section 2.3, the original program ID and PI name for the relevant observations, and the program that developed the HLSP used in this analysis.
[a] Numerous observing programs were used for the ACS HLSPs; see G. D. Illingworth et al. (2013) for details. Finally, we list the relevant PIs and programs for the WFC3/IR filters; however, we note that the HLSPs were only used as references because the F105W, F140W, and F160W images were all reprocessed to create two separate epoch images for each of the aforementioned filters in this work.

3.2. AGN Model

This work employs the AGN semiempirical templates from M. J. Temple et al. (2021). The templates are constructed to reproduce the average Sloan Digital Sky Survey (SDSS)-UKIRT Infrared Deep Sky Survey-Wide-field Infrared Survey Explorer colors of quasars with $0 < z < 5$. Compared to previous quasar catalogs, the M. J. Temple et al. (2021) templates are generated from a more complete sample since the SDSS DR 16 catalog of quasars represents an increased

Table 2
Parameter Space Defined to Generate the Set of Stellar Spectra with BAGPIPES, Which Were Used to Make the Model Grid for Our Bespoke SED Fitting Code

Parameter	Range
IMF	P. Kroupa (2001)
t_i [Myr], $i = 1, 2..., 100$	$t_i = t_{\rm min} \cdot (t_{\rm max}/t_{\rm min})^{(i-1)/(100-1)}$; $t_{\rm min} = 1$, $t_{\rm max} = 10^4$
τ [Myr]	2, 5, 10, 20, 50, 100, 200, 500, 1000, 2000, 5000, 10,000
Metallicity [$Z_\odot$]	0.1, 0.2, 0.5, 1, 2
Ionization Parameter, log U	−2.5

range of luminosities per redshift bin. Additionally, these templates include a diverse population of the strongest rest-frame UV and optical emission lines while maintaining a small number of free parameters. These qualities, in conjunction with the fact that great care has been taken to account for host-galaxy contamination to the quasar continuum, make these templates a valuable tool for SED modeling (M. J. Temple et al. 2021; A. Marshall et al. 2022).

The template incorporates a broken power law to model the UV-optical emission from the accretion disk, blackbody emission of hot dust dominating the near-IR emission, as well as broad and narrow emission lines. Our code generates an AGN model with the publicly available `qsogen` code by setting the template redshift to the known galaxy redshift from crossmatching performed by V. Cammelli et al. (2025). Redshift classifications in V. Cammelli et al. (2025) prioritized spectroscopic redshifts from JADES (A. J. Bunker et al. 2024) and Very Large Telescope/MUSE (R. Bacon et al. 2023), using photometric redshifts from JADES (M. J. Rieke et al. 2023b) and the UVUDF (M. Rafelski et al. 2015) when spectroscopic redshifts were unavailable. Additionally, the "lyForest" parameter, which implements intergalactic medium (IGM) absorption, and the "gflag" parameter, which includes a host-galaxy flux contribution, are all set to "False", and the "lylim" is forced to zero. These choices are made such that we can independently calculate a host-galaxy contribution to the flux and uniformly apply IGM transmission and dust reddening to both components of our combined AGN + SP models.

3.3. Minimization and Model Selection

We simultaneously fit the parameters that govern our stellar models, namely, the duration of the star formation, also known as the e-folding time ($\log_{10}(\tau)$), the age of the SP ($\log_{10}(t_{\rm age})$), a normalization factor for the stellar templates ($\rm norm_{stellar}$), the metallicity ($Z/Z_\odot$), a diffuse reddening parameter, which applies to both the SP and the AGN following the Calzetti Law (D. Calzetti et al. 2000) ($E(B–V)_{\rm diffuse}$), as well as those that define our AGN model, including a normalization factor for the AGN template ($\rm norm_{AGN}$) and a nuclear reddening term following the SMC law (M. L. Prevot et al. 1984), which applies only to the AGN template ($E(B–V)_{\rm AGN}$). For our pure SP model (denoted as the SP model), this corresponds to five free parameters, while for our combined stellar and AGN model (denoted as the AGN + SP model) this gives us a total of seven free parameters. Additionally, our model includes IGM absorption following P. Madau (1995).

In order to determine our best-fit model parameters, we use three steps in sequence. First, the parameter space is explored by an optimizer, namely, NonLinear Least-Squares Minimization and Curve-Fitting for Python, or `lmfit` (M. Newville et al. 2016). The results of this fit are then used to initialize a Markov Chain Monte Carlo (MCMC) Ensemble sampler, namely, `emcee` (D. Foreman-Mackey et al. 2013) to estimate the posterior distributions of our model parameters. Finally, since we expect there to be multiple modes in the posterior distribution and to prevent the scenario where the walkers miss the actual location of the maximum likelihood (corresponding to the "best-fit" model), we use the results from the MCMC fit to inform a final run of `lmfit` in order to allocate the best-fit model parameters to those that minimize the residual of our model. Numerous tests showed that the final fits were significantly improved (i.e., the χ^2 was significantly reduced) when this additional run of `lmfit` was implemented. This final model output is used as our best-fit model for each run.

Operating under the baseline assumption that all of the sources in our sample vary in brightness between epochs due to the presence of an AGN, we test what fraction of these AGN can be recovered from SED fitting alone. We therefore model the same set of photometry for each source with a pure stellar component and for a combined stellar + AGN model. We then compare the pure SP model and the combined (AGN + SP) model for each source to identify those sources that have photometry that is better reproduced by including the AGN templates into our SED fitting. To test this, we define two criteria. First, we calculate the Akaike information criterion (AIC) from

$$\mathrm{AIC} = 2k - 2\log(L), \tag{1}$$

where k is the number of free parameters, and L is the maximum likelihood. The AIC penalizes models with additional free parameters, meaning we can use it to compare our combined model and pure stellar model to determine which set of parameters provides an improved fit to the data. We consider a fit to be statistically improved by including an AGN component if the AIC decreases by at least 6 for the combined model compared to the pure stellar model. This corresponds to a relative uncertainty of

$$\exp\left(\frac{\mathrm{AIC_{AGN+SP}} - \mathrm{AIC_{SP}}}{2}\right) = \exp(-6/2) = 0.0497, \tag{2}$$

suggesting the combined model is ∼0.95 times more likely to minimize the information loss from the "true" model compared to the pure SP model (K. P. Burnham & D. R. Anderson 2002).

Additionally, we employ a second criterion denoted by $\rm AGN_{frac}$, which is also determined from our best-fit AGN + SP model. $\rm AGN_{frac}$ is used to estimate the maximal contribution of the best-fit AGN template to the total flux of the SED in each filter. We convolve the best-fit AGN spectrum with each filter transmission function to determine an "AGN SED," which we divide by the best-fit model SED for the total flux (i.e., AGN + SP) in each filter and take the maximal result from all 26 filters to be $\rm AGN_{frac}$. We then apply the condition

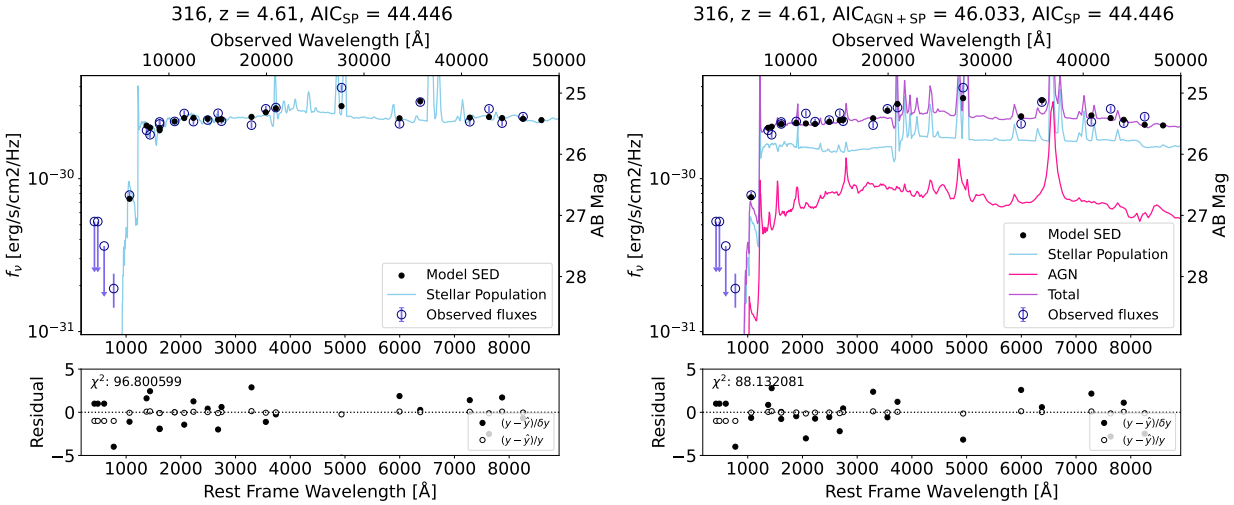

Figure 2. SED fitting results for source 316 at $z = 4.61$ for the pure stellar population (SP) model (left) and the combined (AGN + SP) model (right). These fits are performed on the same set of photometry for this source, namely, in both cases, the WFC3/IR epochs are selected where the variable AGN is in the bright state. The SP is shown in blue, the AGN contribution in pink, and the combined stellar + AGN in purple. The observed data points are plotted in navy, and the corresponding best-fit SED data are represented by the black points. Below, we show the residuals between the best-fit SED points and data for each model in two ways, the black points are the residuals divided by the error in the data, whereas the white points are the residuals divided by the data values. Here, we can see that the AIC resulting from the pure stellar fit (AIC$_{SP}$) is less than the AIC for the combined fit AIC$_{AGN+SP}$, meaning the SED fitting was not successful in retrieving the AGN nature of this source.

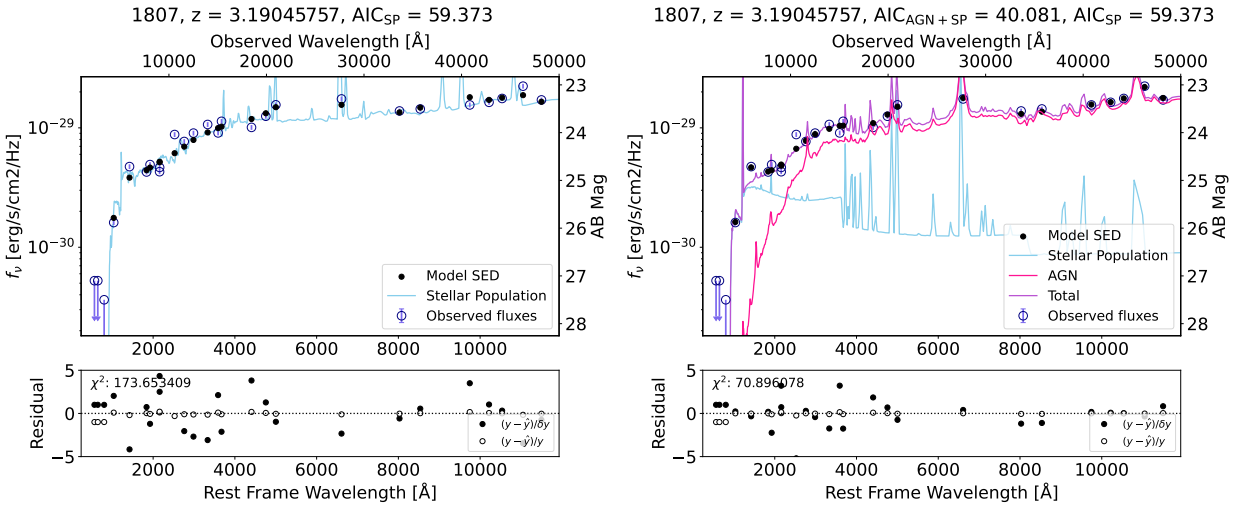

Figure 3. The same as Figure 2 except for source 1807 at $z \simeq 3.19$. This source, however, has an AIC for the combined model, which is less than the AIC for the pure stellar population model, and the difference between these AIC values is > 6, meaning that it is possible to retrieve the AGN nature of this source using our SED fitting. Additionally, this source is a confirmed broad-line emitter from NIRISS spectroscopy presented in M. J. Hayes et al. (2024; see also N. Pirzkal et al. 2024). This provides additional evidence that the SED fitter is able to accurately retrieve AGN contributions to the flux when spectroscopic AGN features are observed. It is also clear that this source has a significant contribution to the flux from the AGN template, reaching 95% in at least one filter. Therefore, this source also meets our AGN$_{frac}$ condition.

that, in order to be successfully retrieved as an AGN via SED fitting, the source must have an AGN$_{frac}$ $>$ 20% to complement the fact that we demand our sources have S/N > 5 in at least eight filters.

Figures 2 and 3 show the fitting results for two sources. In particular, Figure 2 presents both the best-fit pure stellar population model and the best-fit combined model. We can see that, while the total χ^2 is smaller when the AGN template is included, the AIC condition is not met by this source. We would therefore not consider that the AGN nature of this source is retrieved by the SED fitter in this case. However, in Figure 3, the AIC is drastically reduced for the combined model. In this instance, a reasonable fit is recovered using a pure stellar model, but when an AGN is included in the fit, it almost entirely replaces the stellar SED, and the source shows only an excess of starlight at the blue end. In this case, we consider the AGN nature of the source successfully retrieved by SED fitting.

3.4. Parameter Estimation

In the previous subsection, we discuss determining the best-fit model and using statistics from this fit to identify whether our pure stellar model or our combined model best reproduces the observed photometry for our sources. We note that, since our posteriors are expected to be quite complex in seven dimensions, the use of the final `lmfit` result is essential as

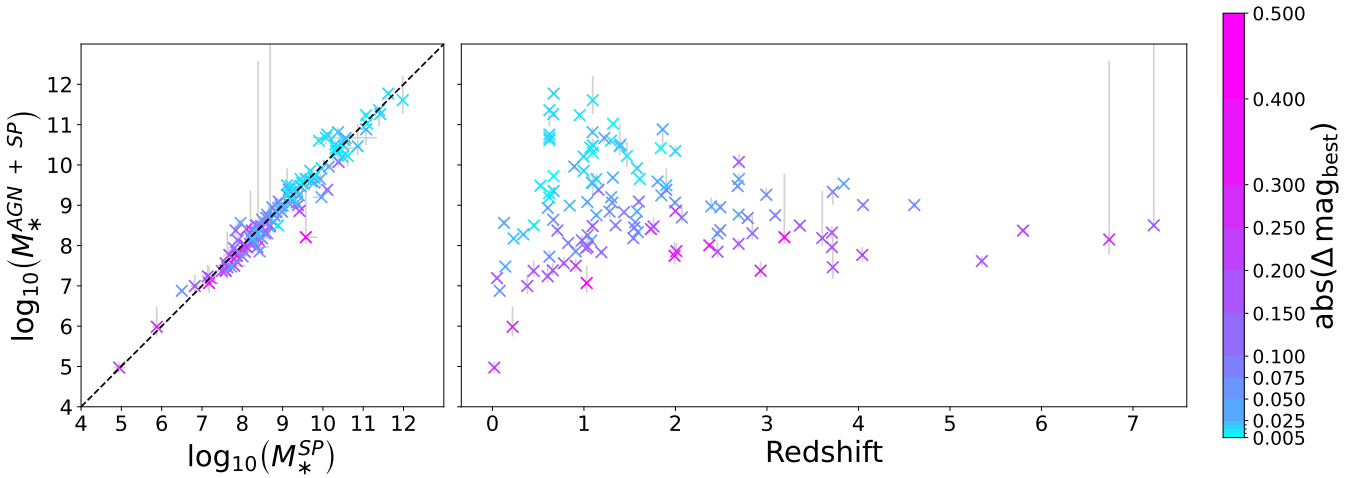

Figure 4. The output stellar mass from the SED fitter when using our combined model, $M_*^{\rm AGN+SP}$, versus the stellar mass when a pure stellar population is used, $M_*^{\rm SP}$, (left) and redshift (right). The points are colored by the largest change in AB magnitude between the WFC3/IR epochs in either F105W, F140W, or F160W, abs(Δ mag$_{\rm best}$). $M_*^{\rm AGN+SP} = M_*^{\rm SP}$ is given by the black-dashed line and shows that the stellar masses typically agree well between runs of the SED fitter.

optimizing the posterior (as is done with the minimizer) is not equivalent to sampling the posterior (as is the case for the MCMC method) when the posterior distributions are not narrow (D. W. Hogg & D. Foreman-Mackey 2018). However, the shape of the posterior becomes important to properly determine the confidence intervals (i.e., the upper and lower limits) on the model parameters of our fits. Therefore, we use the MCMC results for parameter estimation. This means for each source we have both a best-fit model, which we use to determine the AIC and AGN$_{\rm frac}$ conditions, and a most probable model, which we use to estimate the values of our free parameters. Namely, for each of our (maximally) seven free parameters, we take the median of the posterior distribution to be the most probable solution and determine the errors from the 16th and 84th percentiles. These values are used to determine the stellar masses (M_*) and reddening parameters for each of our sources. We also use the resulting parameters from the MCMC fits to generate an AGN spectrum and measure L_{5100} to estimate $M_{\rm BH}$ for each source.

We note that the model parameters may vary between the results from the minimizer and those from the MCMC sampler. However, the final values calculated using both sets of parameters (i.e., $M_{\rm BH}$ and M_*) typically agree within errors between both fit results for a given source. This is discussed further in Appendix C.

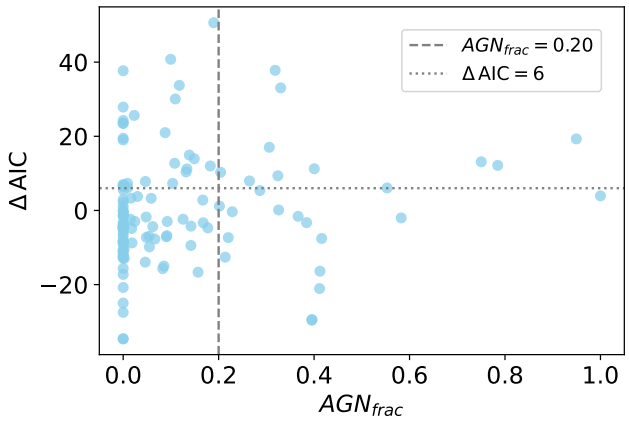

Figure 5. The difference between the Akaike information criterion (AIC) calculated for the best-fit SED modeled with a pure stellar population versus our combined model with a stellar and AGN component (ΔAIC = AIC$_{\rm SP}$ − AIC$_{\rm AGN+SP}$) as a function of AGN$_{\rm frac}$. The horizontal gray-dotted line indicates the ΔAIC = 6 criterion used to define which sources have SEDs that are statistically improved by including an AGN template in the model. The vertical gray-dashed line indicates the AGN$_{\rm frac}$ = 0.2 line; the sources to the right of which meet our AGN$_{\rm frac}$ criterion. We calculate $M_{\rm BH}$ for the sources with AGN$_{\rm frac}$ > 0.2 since these are the sources that have a contribution to the total flux from the best-fit AGN template exceeding 20% in at least one filter. In total, 37 out of 121 variables meet our AIC criterion, 26 out of 121 meet the AGN$_{\rm frac}$ criterion, and 11 out of 121 meet both criteria.

4. Results

4.1. Determining AGN Contribution from SED Fitting

A summary of the stellar masses that result from fitting our full set of 121 variable sources with both a purely SP ($M_*^{\rm SP}$) as well as our combined model featuring both a best AGN template and an SP model ($M_*^{\rm AGN+SP}$) is depicted in Figure 4. The right panel of Figure 4 also shows the stellar mass from our combined model as a function of redshift. Generally, the two sets of models result in stellar masses that agree well between runs of the SED fitter.

The color bar in Figure 4 is a proxy for the variability of the source and is determined by taking the largest change in AB magnitude between two epochs in any of the WFC3/IR filters. The evolution of this variability measurement with stellar mass and redshift is a reflection of the source selection procedure. Here, bright sources that result in larger stellar masses at lower redshifts required a smaller change in flux between epochs to be considered a significant variable in V. Cammelli et al. (2025). For sources approaching the limiting magnitudes of the images (resulting in correspondingly lower stellar masses), the difference in flux between epochs needed to be larger to account for the additional uncertainty in the measured flux. The shape of this distribution reflects the completeness of our source selection and represents our ability to probe lower masses near $z = 0$ than at high redshift for a given magnitude limit. Additionally, Figure 4 is consistent with the known anticorrelation between $M_{\rm BH}$ and variability in that the lower stellar mass systems are more likely to host lower-mass BHs, which typically exhibit higher variability amplitudes (see, e.g., W. Yu et al. 2022; P. Arévalo et al. 2024).

Table 3
A Summary of the Variable Sources Meeting Our AGN_{frac} Condition

ID	R.A.	Decl.	z	z_{type}
2199	53.179405	−27.781833	0.22	p
116	53.163439	−27.799619	0.6649	s
1059	53.157257	−27.785336	0.6676	s
458	53.172081	−27.797478	0.71	p
3902	53.165592	−27.763133	0.8274	s
3976	53.165344	−27.762849	1.03	p
222	53.156769	−27.795656	1.0966	s
1441	53.160980	−27.786578	1.1348	s
3404	53.166354	−27.768660	1.2954	s
1975	53.184353	−27.783443	1.3458	s
1013	53.160445	−27.790442	1.6098	s
3752	53.164102	−27.765497	1.76	p
2156	53.155676	−27.779348	1.8391	s
3005	53.159608	−27.774646	1.9	p
1775	53.174344	−27.782600	1.9982	s
446	53.166077	−27.798129	2.01	p
2460	53.144954	−27.779554	2.68	p
1540	53.180808	−27.786333	2.6900	s
2810	53.183466	−27.776658	2.6933	s
2774	53.183386	−27.776454	2.6933	s
2810	53.183466	−27.776658	2.6933	s
2774	53.183386	−27.776454	2.6933	s
45	53.161165	−27.806155	2.9928	s
1807	53.178511	−27.784108	3.1905	s
3384	53.166094	−27.771261	3.6040	s
258	53.152758	−27.800964	3.72	p
316	53.151454	−27.799838	4.61	p
1511	53.161944	−27.787065	6.74	p

Note. Here, z_{type} indicates whether the source has an available spectroscopic redshift (s) or if only a photometric redshift (p) is available.

We present ΔAIC as a function of AGN_{frac} in Figure 5. The horizontal dotted line indicates where ΔAIC = 6, meaning sources above this dashed line have a statistically improved SED fit when using the AGN + SP model. All sources with an $AGN_{frac} > 20\%$ are located rightward of the vertical gray-dashed line in Figure 5. We present the sources meeting our AGN_{frac} criterion in Table 3.

In total, 37 out of 121 variables meet our AIC criterion, 26 out of 121 meet the AGN_{frac} criterion, and 11 out of 121 meet both criteria. Sources that do not meet our AIC criterion are not necessarily misidentified as AGN in our sample selection. This instead reflects the well-known challenge of identifying AGN purely from their SEDs (e.g., E. Pouliasis et al. 2019; J. Lyu et al. 2022): in these instances, we simply cannot demonstrate statistical evidence for the presence of an AGN from the SED data alone.

In the following analysis, we determine BH properties for the sources that meet the AGN_{frac} criterion. Due to the fact that we are assuming all of our 2.5σ variables are, indeed, varying due to the presence of an AGN, we selected the sample that meet the AGN_{frac} criterion as the SED fitter was able to successfully retrieve a significant AGN contribution to the total flux for these sources.

4.2. Black Hole Mass Estimation

Due to the decomposition of our total SED into separate stellar and AGN contributions, we are able to use the MCMC results to reconstruct our model AGN spectrum to determine L_{5100} by taking the median flux between 4850 and 5350 Å. The calculated L_{5100} can then be used with the relation defined in S. Kaspi et al. (2000) for BH mass as a function of 5100 Å luminosity. To our knowledge, this is the first time that photometric decomposition of stellar and AGN contributions has been leveraged to estimate SMBH masses, and is facilitated in this case by the exquisitely wide bandwidth, 26-filter photometry in the HUDF. S. Kaspi et al. (2000) define this relation by fitting the mass estimates from reverberation mapping (RM) analysis for the mean spectra of a sample of 34 AGN. This gives

$$M_{BH} = 5.71 \times 10^7 \left(\frac{L_{5100}}{10^{44}\ \mathrm{erg\ s^{-1}}}\right)^{0.545} M_\odot. \quad (3)$$

To estimate the errors on M_{BH}, we use the 16th and 84th percentiles from the MCMC results for the $norm_{agn}$ parameter since the luminosity we measure from the model spectrum will be proportional to its normalization. We do not include the intrinsic scatter of the relation in our error propagation. However, we include an error bar in the top left corner of Figure 6 that is representative of the intrinsic scatter of the relation from S. Kaspi et al. (2000). We calculated this via the rms deviation of the data presented in Table 7 of S. Kaspi et al. (2000). We find this rms deviation to be 0.495 dex compared to the typically assumed 0.3 dex associated with scaling relations from J. E. Greene & L. C. Ho (2005; e.g., R. Maiolino et al. 2024a; although there is some evidence that the scatter could be as high 0.5–0.7 dex; for the J. E. Greene & L. C. Ho 2005 relations when applied to objects at high-z; G. Fonseca Alvarez et al. 2020; R. Abuter et al. 2024). It is expected that the intrinsic scatter of the S. Kaspi et al. (2000) relation will be larger as it depends only on the luminosity at 5100 Å, and the luminosity will correlate with both M_{BH} and the Eddington ratio. Further considerations regarding the associated uncertainties with our M_{BH} estimates are discussed in Section 5. The tabulated results for the various AGN criteria, L_{5100}, M_{BH}, and M_*, are presented in Table 4.

4.3. Source 1511

Our highest-redshift variable source meeting our AGN_{frac} condition has been previously studied in multiple works, and in this section, we will discuss our results in the context of previous literature.

Source 1511 was originally presented in M. J. Hayes et al. (2024) as source 1052123. It has a photometric redshift of 6.74, and interestingly, our SED fitter finds that the photometry from this source is consistent with a contribution almost entirely dominated by a best-fit M. J. Temple et al. (2021) AGN template. C. DeCoursey et al. (2025) report a spectrum from DDT Program 6541 (PI: E. Egami) for this source that they claim is not well matched by any supernova, galaxy, or AGN template at $5 < z < 7$, and is instead fit best by a late-type star at $z \sim 0$. Our SED fitting results and photometry from 26 filters do appear to be consistent with an AGN template, so we do not remove this source from our sample. Using these best-fit results, we retrieve an $AGN_{frac} = 1$. This is slightly lower when we instead consider our MCMC results, from which we derive a lower limit on the BH mass of $\log_{10}(M_{BH}/M_\odot) > 7.36$. The stellar mass is not well

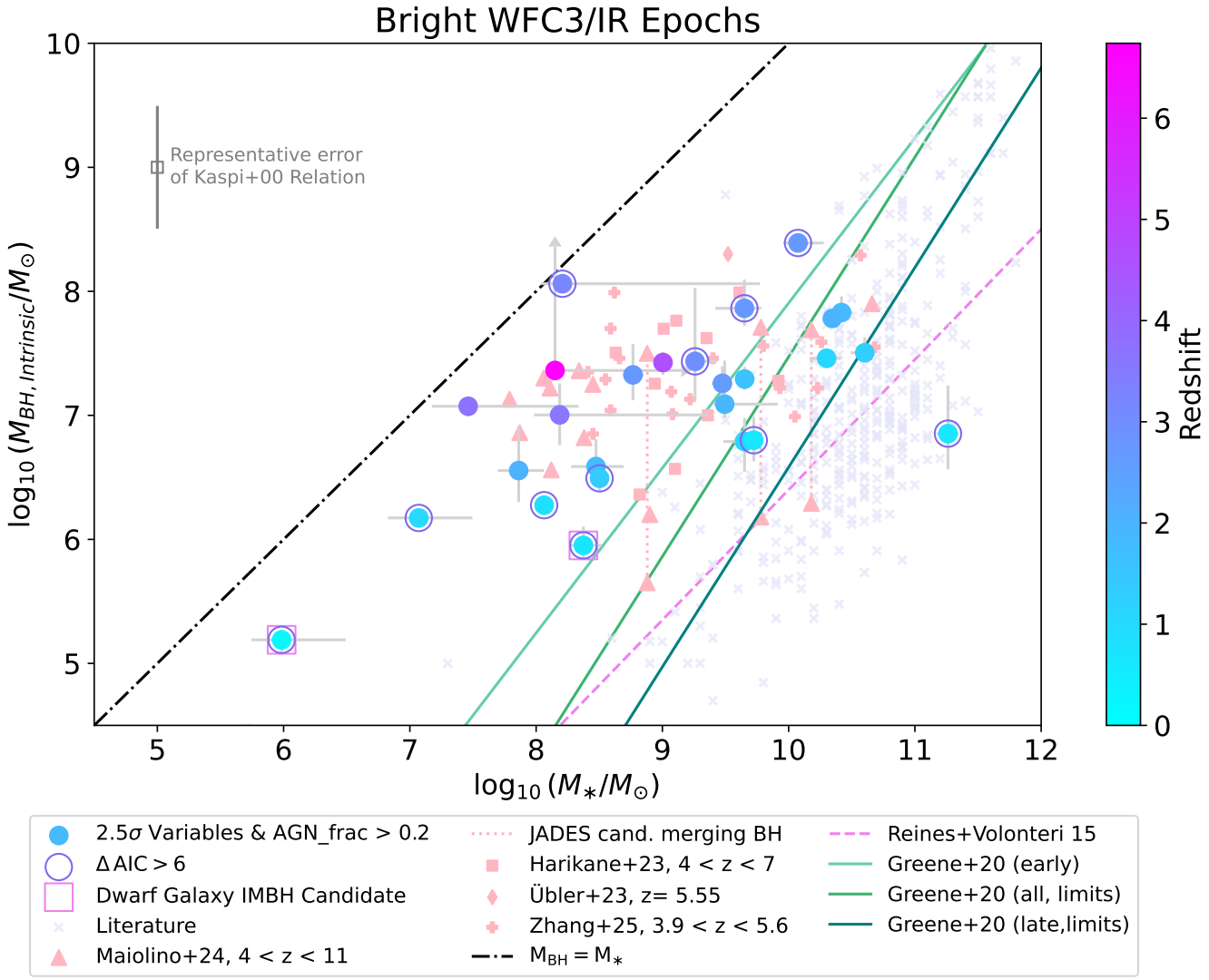

Figure 6. Black hole masses calculated from the S. Kaspi et al. (2000) relation utilizing the luminosity at 5100 Å in the AGN spectrum resulting from the parameters determined from the MCMC SED fit as a function of stellar mass for each variable meeting the AGN_{frac} condition. Sources that also meet our ΔAIC condition are outlined by purple circles. Sources are colored by redshift, and the L_{5100} values used to calculate M_{BH} are determined from spectra that have undergone a reddening correction calculated from the MCMC results for $E(B–V)_{diffuse}$ and $E(B–V)_{AGN}$ as well as IGM absorption along the line of sight. The scaling relation between black hole mass and stellar mass determined from a sample of 262 $z < 0.055$ BL-AGN from A. E. Reines & M. Volonteri (2015) is shown as the pink-dashed line as well as similar scaling relations from J. E. Greene et al. (2020) in shades of green. The 1:1 line for M_{BH} and M_* is plotted as the dashed–dotted black line. Low-redshift objects with values for black hole mass and stellar mass from the literature are included from the table compiled by I. Zaw et al. (2020). These are marked by the lilac "x" symbols. Finally, we offer a direct comparison to black hole masses determined from fitting broad Hα emission lines from R. Maiolino et al. (2024a; pink triangles), Y. Harikane et al. (2023; pink squares), H. Übler et al. (2023; pink diamonds), and J. Zhang et al. (2025; pink crosses). Our two IMBH candidates identified in dwarf galaxies are marked by the pink boxes. Additionally, we show a representative error bar reflecting the intrinsic scatter of the relation from S. Kaspi et al. (2000) used to estimate M_{BH}, which is found to be ∼0.495 dex.

constrained by the SED fitter, and we again provide a lower limit of $\log_{10}(M_*/M_\odot) > 8.15$. This source is likely best described by a bright AGN with very little contribution to its total flux from any SP. Given that we do not include individual stellar templates in our suite of SED models and that the errors on the resulting MCMC parameters remain large, we cannot rule out the stellar classification from C. DeCoursey et al. (2025); however, we treat 1511 as a $z_{phot} \simeq 6.74$ AGN candidate in the remainder of the analysis in this work.

5. Discussion

5.1. Mass Calculations with L_{5100}

As shown in Figure 6 and summarized in Table 4, our modeling recovers BH masses that range from the intermediate mass regime at $\sim 10^5\,M_\odot$ through to the supermassive at $\gtrsim 10^8\,M_\odot$.

S. Kaspi et al. (2000) detail many caveats that enter into the determination of M_{BH} using the scaling relations presented therein, including the assumptions that are necessary for deriving physical parameters from the properties of Balmer emission lines. However, additional considerations are also relevant when applying this relation to our sample specifically. First, the population studied here is not representative of the sample for which the relation was derived. In particular, we probe sources with systematically fainter L_{5100} than S. Kaspi et al. (2000). Our median value is $\sim 10^{42.9}\,\mathrm{erg\,s^{-1}}$, and we probe down to $L_{5100} \sim 10^{39}\,\mathrm{erg\,s^{-1}}$ versus a median of $\sim 10^{44.2}\,\mathrm{erg\,s^{-1}}$ from S. Kaspi et al. (2000) where the source with the lowest $L_{5100} \sim 10^{41}\,\mathrm{erg\,s^{-1}}$. S. Kaspi et al. (2000)

Table 4
A Summary of the Variable Sources Meeting Our AGN_{frac} Condition and the Relevant Quantities Determined from Our SED Fitting Code for the BH and Host Galaxy

ID	AGN_{frac}	AIC_{AGN+SP}	AIC_{SP}	L_{5100} (erg s^{-1})	$\log(M_{BH,int}/M_{\odot})$	$\log(M_*/M_{\odot})$	$E(B-V)_{diffuse}$	$E(B-V)_{AGN}$
2199	0.75	13.39	26.50	1.95×10^{39}	$5.19^{+0.08}_{-0.10}$	$5.98^{+0.51}_{-0.24}$	$0.07^{+0.07}_{-0.05}$	$0.90^{+0.64}_{-0.63}$
116	0.32	-8.06	29.74	2.19×10^{42}	$6.85^{+0.39}_{-0.29}$	$11.26^{+0.09}_{-0.09}$	$0.06^{+0.03}_{-0.03}$	$0.61^{+0.94}_{-0.41}$
1059	0.32	12.57	21.93	1.75×10^{42}	$6.80^{+0.19}_{-0.17}$	$9.72^{+0.07}_{-0.06}$	$0.43^{+0.04}_{-0.03}$	$0.88^{+0.73}_{-0.62}$
458	0.26	46.35	54.31	4.87×10^{40}	$5.95^{+0.15}_{-0.12}$	$8.37^{+0.14}_{-0.11}$	$0.08^{+0.05}_{-0.05}$	$1.08^{+0.65}_{-0.77}$
3902	0.40	46.47	57.71	1.92×10^{41}	$6.28^{+0.08}_{-0.08}$	$8.06^{+0.04}_{-0.04}$	$0.04^{+0.02}_{-0.02}$	$1.46^{+0.40}_{-0.67}$
3976	0.78	27.27	39.43	1.24×10^{41}	$6.17^{+0.07}_{-0.06}$	$7.07^{+0.43}_{-0.24}$	$0.05^{+0.06}_{-0.03}$	$0.00^{+0.00}_{-0.00}$
222	0.40	35.30	5.88	2.85×10^{43}	$7.46^{+0.08}_{-0.08}$	$10.30^{+0.12}_{-0.13}$	$0.37^{+0.02}_{-0.02}$	$0.00^{+0.00}_{-0.00}$
1441	0.20	39.55	40.73	1.68×10^{42}	$6.79^{+0.19}_{-0.24}$	$9.65^{+0.13}_{-0.17}$	$0.21^{+0.02}_{-0.03}$	$0.02^{+0.08}_{-0.02}$
3404	0.41	63.98	47.59	3.45×10^{43}	$7.50^{+0.12}_{-0.05}$	$10.60^{+0.05}_{-0.11}$	$0.20^{+0.02}_{-0.02}$	$0.02^{+0.96}_{-0.02}$
1975	0.33	10.47	43.53	4.79×10^{41}	$6.49^{+0.12}_{-0.11}$	$8.50^{+0.06}_{-0.07}$	$0.07^{+0.03}_{-0.07}$	$1.04^{+0.57}_{-0.48}$
1013	0.40	47.95	18.35	1.41×10^{43}	$7.29^{+0.10}_{-0.09}$	$9.65^{+0.04}_{-0.06}$	$0.10^{+0.03}_{-0.02}$	$0.06^{+0.95}_{-0.05}$
3752	0.33	35.67	35.80	7.15×10^{41}	$6.59^{+0.22}_{-0.16}$	$8.47^{+0.22}_{-0.20}$	$0.06^{+0.07}_{-0.04}$	$0.96^{+0.70}_{-0.85}$
2156	0.38	23.83	20.55	1.36×10^{44}	$7.83^{+0.13}_{-0.06}$	$10.42^{+0.09}_{-0.10}$	$0.29^{+0.02}_{-0.02}$	$0.03^{+0.41}_{-0.03}$
3005	0.42	28.97	21.42	5.99×10^{42}	$7.09^{+0.35}_{-0.11}$	$9.49^{+0.42}_{-0.09}$	$0.14^{+0.04}_{-0.09}$	$0.27^{+1.36}_{-0.25}$
1775	0.41	32.65	11.58	1.11×10^{44}	$7.78^{+0.07}_{-0.05}$	$10.35^{+0.12}_{-0.08}$	$0.34^{+0.03}_{-0.02}$	$0.00^{+0.01}_{-0.00}$
446	0.22	-13.76	21.09	6.24×10^{41}	$6.55^{+0.36}_{-0.25}$	$7.86^{+0.20}_{-0.17}$	$0.16^{+0.08}_{-0.08}$	$1.25^{+0.55}_{-0.75}$
2460	0.29	35.23	40.59	1.22×10^{43}	$7.26^{+0.14}_{-0.11}$	$9.48^{+0.07}_{-0.08}$	$0.14^{+0.02}_{-0.02}$	$0.07^{+0.11}_{-0.05}$
1540	0.21	76.53	63.92	1.62×10^{43}	$7.33^{+0.25}_{-0.20}$	$8.77^{+0.09}_{-0.08}$	$0.04^{+0.04}_{-0.03}$	$0.72^{+0.38}_{-0.35}$
2810	0.55	42.22	48.29	1.45×10^{45}	$8.39^{+0.06}_{-0.06}$	$10.07^{+0.20}_{-0.12}$	$0.73^{+0.03}_{-0.04}$	$0.52^{+0.20}_{-0.11}$
2774	0.31	-2.67	14.37	1.57×10^{44}	$7.86^{+0.23}_{-0.14}$	$9.65^{+0.13}_{-0.23}$	$0.24^{+0.03}_{-0.07}$	$0.23^{+0.10}_{-0.12}$
2810	0.55	42.22	48.29	1.45×10^{45}	$8.39^{+0.06}_{-0.06}$	$10.07^{+0.20}_{-0.12}$	$0.73^{+0.03}_{-0.04}$	$0.52^{+0.20}_{-0.11}$
2774	0.31	-2.67	14.37	1.57×10^{44}	$7.86^{+0.23}_{-0.14}$	$9.65^{+0.13}_{-0.23}$	$0.24^{+0.03}_{-0.07}$	$0.23^{+0.10}_{-0.12}$
45	0.20	46.59	56.88	2.57×10^{43}	$7.44^{+0.59}_{-0.32}$	$9.26^{+0.18}_{-0.07}$	$0.04^{+0.06}_{-0.02}$	$1.12^{+0.73}_{-0.95}$
1807	0.95	40.08	59.37	3.62×10^{44}	$8.06^{+0.02}_{-0.03}$	$8.21^{+1.56}_{-0.17}$	$0.03^{+0.02}_{-0.02}$	$0.31^{+0.02}_{-0.02}$
3384	0.23	2.93	2.58	4.15×10^{42}	$7.00^{+0.25}_{-0.24}$	$8.19^{+1.18}_{-0.20}$	$0.04^{+0.06}_{-0.03}$	$0.26^{+1.11}_{-0.25}$
258	0.58	32.71	30.71	5.57×10^{42}	$7.07^{+0.06}_{-0.08}$	$7.46^{+0.87}_{-0.29}$	$0.02^{+0.02}_{-0.02}$	$0.02^{+0.03}_{-0.01}$
316	0.37	46.03	44.45	2.47×10^{43}	$7.43^{+0.08}_{-0.10}$	$9.00^{+0.08}_{-0.07}$	$0.02^{+0.02}_{-0.01}$	$0.02^{+0.02}_{-0.01}$
1511	1.00	26.97	30.91	1.89×10^{43}	>7.36	> 8.15	$0.01^{+0.73}_{-0.01}$	$0.01^{+0.56}_{-0.01}$

Note. Here, L_{5100} refers to the luminosity at 5100 Å measured from the corrected spectra, which is used to determine the reported $M_{BH,int}$ values. The errors for $M_{BH,int}$ do not include the intrinsic scatter introduced by using the relation from S. Kaspi et al. (2000); however, the rms deviation of this relation was calculated here from data in Table 7 of S. Kaspi et al. (2000) to be ∼0.495 dex. All values reported except AIC_{SP} are determined from the results of the SED model corresponding to our combined (AGN + SP) model using the set of photometry that includes the measurements taken at the bright epochs in the WFC3/IR filters. AIC_{SP} is reported from the SED run that modeled the same photometry, however, using only the stellar population model.

does warn that using the relations dependent on luminosity determinations for fainter sources would lead to increased contributions from the host-galaxy light. However, to the first order, this effect should be mitigated by our approach of decomposing the stellar and AGN light in the SED modeling. Additionally, many sources in our sample are also at significantly higher redshift than the $z < 1$ sample from S. Kaspi et al. (2000). It is not yet known whether the relations that can be used to determine BH masses at low redshift are accurate also at high redshift (H. Übler et al. 2023; R. Maiolino et al. 2024a). Further, although it was found that M_{BH} and L_{5100} had a Pearson linear correlation coefficient of 0.646 at a significance level of 3.7×10^{-5}, Equation (3) is determined from a low-number sample featuring significant scatter. J. Kormendy & L. C. Ho (2013) also emphasize that all mass determinations based on virialized motion in the broad-line region (BLR) depend on the scaling of masses such that they obey the robust M_{BH}–σ_* relation. This is a shortcoming of this method as the M_{BH}–σ_* relations used were derived incorporating sources featuring both classical bulges and pseudobulges, despite M_{BH} not correlating with pseudobulges (J. Kormendy & L. C. Ho 2013). Depending on the galaxy sample used to define the M_{BH}–σ_* sample, this can introduce an uncertainty up to a factor of 2 (L. C. Ho & M. Kim 2016; J. E. Greene et al. 2020). Finally, we are applying this function to a model spectrum resulting from photometric SED analysis, rather than an observed spectrum.

With this in mind, the resulting BH mass estimates for our variable sources are consistent with those determined in other works at similar redshifts that utilize the luminosity and FWHM of the broad component of Hα (see comparison to JWST high-z BL-AGN masses in Figure 6).

The BH masses estimated here are also consistent with the trend toward overmassive BHs with increasing redshift frequently observed with JWST-detected high-z SMBHs. This is despite the fact that we use a different method to determine the BH mass, which, in this case, is independent of Balmer emission line profiles.

Additionally, we are able to directly compare the BH mass calculated using L_{5100} to that using the luminosity and FWHM of Hβ for one source, namely, source 1807. The best-fit SED for this source is shown in the right panel of Figure 3, and it is identified as a BL-AGN in an NIRISS spectrum (M. J. Hayes et al. 2024; see also N. Pirzkal et al. 2024). We find an Hβ

luminosity ($L_{H\beta}$) of 9.5×10^{41} erg s^{-1} with an S/N ~ 8 and an FWHM (FWHM$_{H\beta}$) of $\simeq 3600 \pm 500$ km s^{-1}. With these measurements, we apply the relation from J. E. Greene & L. C. Ho (2005), which is given as

$$M_{\rm BH} = 2.4 \times 10^6 \left(\frac{L_{H\beta}}{10^{42}\ {\rm erg\ s^{-1}}} \right)^{0.59} \times \left(\frac{{\rm FWHM}_{H\beta}}{10^3\ {\rm km\ s^{-1}}} \right)^2 M_\odot. \quad (4)$$

Using this relation, we find $\log_{10}(M_{\rm BH}/M_\odot) = 7.48 \pm 0.13$ if we consider the uncertainties in our measured Hβ line properties, but excluding the intrinsic scatter from the scaling relation. This is compared to the value we retrieve using L_{5100}, which gives $\log_{10}(M_{\rm BH}/M_\odot) = 8.06^{+0.02}_{-0.03}$. This means that the $M_{\rm BH}$ calculated for this source using these two methods agrees by a factor of $\sim$3.5. Differences in calculated $M_{\rm BH}$ are expected between alternate methods (K. T. Korista & M. R. Goad 2004; R. Abuter et al. 2024; E. Dalla Bontà et al. 2025). E. Dalla Bontà et al. (2025) examined the comparison between single-epoch methods to determine $M_{\rm BH}$ and compared them to the results using interferometry to spatially resolve the rotation of broad-line regions using the GRAVITY instrument on the ESO VLTI (e.g., Gravity Collaboration et al. 2018). The level of agreement between our method using L_{5100} and the line properties of Hβ is at a similar level to the agreement in $M_{\rm BH}$ calculated for the quasar 3C 273 using the luminosity and FWHM of Hβ, which gave $\log_{10}(M_{\rm BH}/M_\odot) = 9.383 \pm 0.372$ (S. Kaspi et al. 2000), and that determined from GRAVITY, $\log_{10}(M_{\rm BH}/M_\odot) = 8.41 \pm 0.18$ (Gravity Collaboration et al. 2018) when the errors on the measurements are considered. The two masses calculated for 1807 also show a similar level of agreement as was found for 3C 273 when comparing the masses retrieved using Hβ and Hα ($\log_{10}(M_{\rm BH,H\alpha}/M_\odot) = 9.403 \pm 0.328$, from S. Kaspi et al. 2000).

Although we can only make this comparison for a single source, the agreement found between the $M_{\rm BH}$ determined using these separate methods for source 1807 suggests that masses calculated from the L_{5100} relation in S. Kaspi et al. (2000) can be used to provide reliable estimates for the BH masses of our variable sources.

5.2. The M_{BH}–M_* Relation

We plot the 26 sources meeting our AGN$_{\rm frac}$ condition in the $M_{\rm BH}$–M_* plane in Figure 6. Sources from this work are compared to the corresponding BH and stellar masses determined for low-z AGN from the catalog compiled by I. Zaw et al. (2020) as well as the masses calculated for the BL-AGN at $4 < z < 7$ from recent studies utilizing data from JWST (Y. Harikane et al. 2023; H. Übler et al. 2023; R. Maiolino et al. 2024a; J. Zhang et al. 2025). The scaling relation derived from local BL-AGN at $z < 0.055$ from A. E. Reines & M. Volonteri (2015) as well as those from J. E. Greene et al. (2020) is also included. It is clear that our sources agree with the trends observed by other recent studies probing high-redshift SMBH masses showing that BHs appear to become overmassive with respect to the stellar mass of their host galaxies at $z \gtrsim 4$ (e.g., Y. Harikane et al. 2023; H. Übler et al. 2023; R. Maiolino et al. 2024a; J. Zhang et al. 2025). The agreement of trends in SMBH masses determined in this work and those from recent works utilizing JWST observations is additionally interesting due to the fact that we have used a method independent of those used in other studies. The other works all utilize single-epoch spectroscopy to derive BH masses based on the width of broad lines, whereas our method uniquely relies on the decomposition of our SEDs into their component parts, allowing us to use only the luminosity at 5100 Å determined from our SED model AGN spectra. The works utilizing the properties of broad lines typically utilize the scaling relations originally derived in J. E. Greene & L. C. Ho (2005), which translates the virial mass system from S. Kaspi et al. (2000) derived using RM into a system that depends only on observations of broad Hα. These results are often compared to the scaling relations derived from A. E. Reines & M. Volonteri (2015), which follows the approach outlined in J. E. Greene & L. C. Ho (2005) to define a relation for their sample of SDSS broad Hα emitters. All of which, therefore, assume the BLR is in virial equilibrium and that the relations for $M_{\rm BH}$ that appear to hold at low redshift are also applicable at high redshift (H. Übler et al. 2023; R. Maiolino et al. 2024a). These are also assumptions intrinsic to the scaling relation with L_{5100} from S. Kaspi et al. (2000) since the masses originally used to produce this scaling relation were calculated from broad emission lines. Previous studies have reported systematic uncertainties in the relations used to determine $M_{\rm BH}$ from single-epoch measurements leading to mass disparities up to factors of $\sim$1.5–2.25 (G. Fonseca Alvarez et al. 2020; R. Abuter et al. 2024; E. Dalla Bontà et al. 2025).

As mentioned by previous works, BH masses at higher redshifts being more overmassive than those at low redshift could imply more rapid growth of central SMBHs at early cosmological times. We examine the implication this could have on seeding mechanisms for BHs in the early Universe further in Section 5.4.

5.2.1. The Effects of Reddening on Black Hole Mass

Due to the nature of our SED fitting code, which works on the premise of spectral decomposition, we are able to fit two extinction parameters. One applies globally to the SP and the central AGN, $E(B\text{–}V)_{\rm diffuse}$, and the other is a nuclear reddening term that is only applied to the AGN spectrum, $E(B\text{–}V)_{\rm AGN}$. This means we are able to accurately correct for the reddening at each wavelength of our AGN spectrum using these reddening values and the Calzetti (D. Calzetti et al. 2000) and SMC (M. L. Prevot et al. 1984) extinction laws, respectively.

In the left panel of Figure 7, we plot the difference between the logarithm of the BH masses we estimate when the AGN spectra have been corrected for reddening and IGM absorption ($M_{\rm BH,Intrinsic}$) and the masses calculated from the uncorrected spectra ($M_{\rm BH,Observed}$). Our results show that when estimating the mass from the uncorrected luminosity at 5100 Å the masses can be underestimated by factors of up to 10, with a standard deviation on the difference between estimates of $\sim$0.36. This indicates the potential importance of applying accurate reddening corrections in order to estimate BH masses. An additional consideration is that the relations derived by S. Kaspi et al. (2000) use spectrophotometry that was not corrected for reddening, and it is unlikely that all of their RM sources are dust-free. This obscuration is a possible contributor to the large scatter that is seen on single-epoch

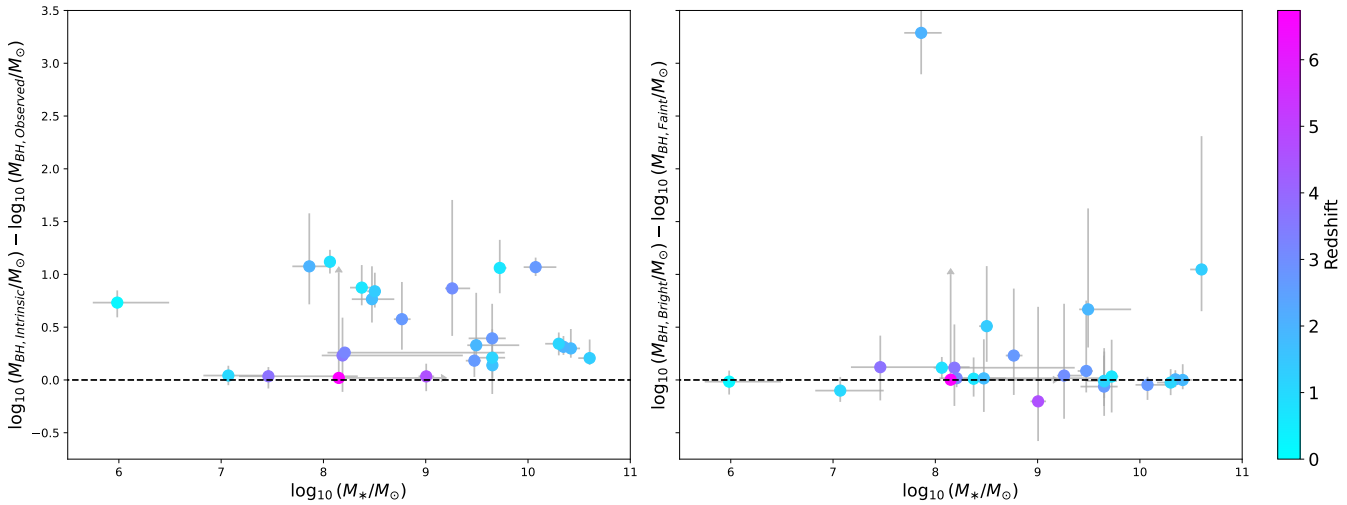

Figure 7. Left: the difference in $M_{\rm BH}$ resulting from the SED model AGN spectra when corrected for reddening and IGM absorption ($M_{\rm BH,Intrinsic}$) and the $M_{\rm BH}$ resulting from the uncorrected spectra ($M_{\rm BH,Observed}$) as a function of M_*. The sources that have large deviations from the black $M_{\rm BH,Intrinsic} = M_{\rm BH,Observed}$ line demonstrate the importance of accurately correcting for reddening when determining $M_{\rm BH}$. Right: the difference in the $M_{\rm BH}$ calculated when we run our SED fitter on the set of photometry containing WFC3/IR fluxes from the epochs where the AGN is bright ($M_{\rm BH,Bright}$) and the $M_{\rm BH}$ resulting from the SED run when the faint WFC3/IR epochs are used ($M_{\rm BH,Faint}$) as a function of M_*. Large deviations from the $M_{\rm BH,Bright} = M_{\rm BH,Faint}$ line show that the intrinsic variability of the AGN can have a significant impact on the estimated $M_{\rm BH}$.

luminosity–$M_{\rm BH}$ calibrations, which we here estimate to be on the order of a factor of $\simeq$3, albeit in a sample much fainter than those used to derive the calibrations.

5.2.2. The Effects of Variability on Black Hole Mass

As well as running two different sets of models for each source, we also test two sets of photometry. Since we have three WFC3/IR filters each with two epochs, we construct two sets of photometric catalogs. The first contains F105W/F140W/F160W fluxes from the epochs where each source is detected to be faint, while the second includes the fluxes from the epochs where the sources are bright.

By comparing the estimated BH masses for our sample using the SED fits performed on the two sets of photometry, we can examine the effects of variability on our SED fitting results. Of course, the BH masses between epochs must, in reality, be almost entirely unchanged due to the small time lapse between observations. Thus, changes observed in the calculated masses reflect the ability of SED modeling to retrieve an AGN contribution to the total flux when the AGN is observed in its faint state. We compare the difference in $M_{\rm BH}$ calculated from SED results performed on these two sets of photometry in the right panel of Figure 7. In many cases, it is observed that, without the bright epochs from WFC3/IR, the recovered BH masses are significantly smaller, and the large error bars resulting from adding the two $M_{\rm BH}$ errors in quadrature indicate that the BH mass is not well constrained by the SED fitting when the faint epoch photometry is used. This suggests that the bright phase of the variability is necessary for these sources to be recovered as AGN using our AIC and $\rm AGN_{frac}$ conditions. Therefore, it can be understood that it may be difficult to recover AGN via SED fitting without considering variability and that, if, by chance, the AGN is observed only when it is in its faint state, the SED may falsely underestimate the AGN contribution to the total flux. It also highlights the fact that variability is an important tool for identifying AGN as a significant fraction of the AGN identified via variability did not meet the requirements of our AIC and $\rm AGN_{frac}$ conditions to be correctly identified as AGN from SED fitting alone.

5.3. Dwarf Galaxies with Overmassive Black Holes

Dwarf galaxies hosting AGN offer a unique opportunity to gain further information about the population of BHs at low redshift overall. In particular, these lower-mass BHs are important for probing the overall number density of BHs, understanding the BH occupation fraction and can provide powerful constraints for the BH mass function. All of which can inform models that seek to predict the formation and coevolution of BHs in galaxies across cosmic time.

Interestingly, two of our sources at $z \lesssim 1$ occupy the dwarf galaxy regime with $M_* < 3 \times 10^9 M_\odot$ and have $M_{\rm BH} < 10^6 M_\odot$. We classify these objects as IMBH candidates and see that they are also overmassive BHs with respect to the calculated stellar masses of their hosts. This is consistent with literature, which has found that BHs residing in dwarf galaxies occupy a similar region of the $M_{\rm BH}$–M_* plane as the high-z SMBH discovered by JWST (C. J. Burke et al. 2022; M. Mezcua et al. 2023; M. Siudek et al. 2023; H. Übler et al. 2023).

However, we note that the overmassive nature of these BH estimates could also be due to the use of quasar templates, which may not be representative of AGN found in dwarf galaxies. To examine the impact of our chosen templates on these two dwarf galaxies, we compare the results obtained when we instead apply the low-luminosity AGN (LLAGN) module implemented in the developer version of CIGALE and presented in I. E. López et al. (2024). In both cases, CIGALE identifies an AGN contribution to the SEDs of these objects. The best models resulting from this fitting estimate that sources 458 and 2199 have $\log(M_*/M_\odot) = 8.13 \pm 0.03$ and $\log(M_*/M_\odot) = 5.67 \pm 0.33$, respectively. This means that the best-fit values from the CIGALE results and the fitter presented in this work have stellar masses that agree to within a factor of $\sim$1.75 for source 458 while the results agree within errors for source 2199.

We then apply the same methodology to the best-fit AGN spectrum from the CIGALE runs to determine BH mass estimates from the measured luminosity at 5100 Å. In both cases, the values for L_{5100} are lower for the CIGALE results than those listed in Table 4, meaning the BH masses are also reduced. For source 458, $\log(M_{\rm BH}/M_{\odot}) = 3.78$; and for source 2199, $\log(M_{\rm BH}/M_{\odot}) = 4.46$. This does indicate that using quasar templates for these low-mass systems results in overmassive predictions of the BHs residing within them. We maintain, however, that the SED fitter successfully identified the presence of these low-mass BHs within these dwarf galaxies using the quasar templates from M. J. Temple et al. (2021) and that this identification is further supported by the contribution found using the LLAGN module in CIGALE.

Regardless of whether these BHs are truly overmassive, the detection of these objects exemplifies how variability can be leveraged to detect BHs in dwarf galaxies. Assuming the results from our fitter, our selection of dwarf galaxies have BH masses $10^5 < M_{\rm BH}/M_{\odot} < 10^6$. Even if overpredicted, these BH masses are systematically lower than the BH masses computed for 25 out of 155 dwarf galaxies exhibiting broad Hα emission lines in A. E. Reines et al. (2013), which had $10^{8.5} < M_{\rm BH}/M_{\odot} < 10^{9.5}$ using the approach from J. E. Greene & L. C. Ho (2005) to determine M_{BH} from the properties of the Hα emission line. This suggests that variability is able to probe lower-mass BHs in dwarf galaxies and could be a unique and important approach for identifying BHs in dwarf galaxies. This was also suggested in the study by E. Kimbro et al. (2025), which used bulge masses determined from a morphological study of photometrically variable dwarf galaxies to determine BH masses. The masses determined by E. Kimbro et al. (2025) were systematically even lower than our dwarf galaxy BH masses at $10^3 < M_{\rm BH}/M_{\odot} < 10^5$.

Additionally, E. J. Wasleske & V. F. Baldassare (2023) found that, for their sample of 23 UV variable AGN candidates in active low-mass galaxies, 11 out of 23 featured X-ray excess typical of AGN. They further identified a sample of sources that were both UV variable and X-ray bright that did, however, not feature any spectroscopic signatures typically found in the optical for active BHs. This further indicates that variability could be an important tool for probing the lower-mass end of the BH mass function since it has been shown that BH indicators that work for more massive galaxies often fail to identify BHs in dwarf galaxies.

5.4. Implications for Black Hole Seeding

From our sample of variables meeting the $\rm AGN_{frac}$ condition, a single source, namely, source 1511, has $z_{\rm phot} > 6$. We calculate a lower limit on $\log_{10}(M_{\rm BH}/M_{\odot}) > 7.36$ and plot this mass as a function of redshift along with masses from various $z > 6$ AGN from the literature in Figure 8 (Y. Harikane et al. 2023; V. Kokorev et al. 2023; R. L. Larson et al. 2023; S. Tacchella et al. 2023; L. J. Furtak et al. 2024; R. Maiolino et al. 2024a, 2024b; R. Tripodi et al. 2025; H. B. Akins et al. 2025; X. Lin et al. 2026; R. P. Naidu et al. 2025; A. J. Taylor et al. 2025). We reproduce Figure 6 from A. J. Taylor et al. (2025) by overplotting the evolution of a light mass seed and heavy mass seed following a simplified Eddington-limited BH growth model. Light seeds are formed at $10^2 M_{\odot}$, and the bounds of the lilac-shaded region correspond to the evolution of a light seed formed at $z = 30$ and $z = 15$. As in A. J. Taylor et al. (2025), for both light seeds, formation is followed by 100 Myr of no growth due to heating of the surrounding gas by the stellar progenitor of the seed (N. Yoshida 2006; J. L. Johnson & V. Bromm 2007) before immediately accreting with $f_{\rm edd} = 1$. The bounds of the magenta-shaded region correspond to a heavy seed formed at $10^4 M_{\odot}$ between $z = 25$ and $z = 15$, which undergoes accretion with $f_{\rm edd} = 1$ immediately. We note that differences in the shaded regions from A. J. Taylor et al. (2025) are due to the slightly different cosmology used in this work. As shown in Figure 8, the lower limit of the mass for source 1511 is consistent with a light seed growing at constant Eddington-limited accretion until $z = 6$ (Z. Haiman & A. Loeb 2001; P. Madau & M. J. Rees 2001; M. Volonteri et al. 2003; Y. Li et al. 2007; K. Inayoshi et al. 2020). Additionally, our source has a BH mass consistent with the other $6 < z < 7$ SMBH from Y. Harikane et al. (2023), R. Maiolino et al. (2024a), and X. Lin et al. (2026) as well as those with $z < 7.5$ from L. J. Furtak et al. (2024) and H. B. Akins et al. (2025). This result would suggest that at $6 \lesssim z \lesssim 7.5$ SMBH that appear to be overmassive in the $M_{\rm BH}$–M_* plane do not necessarily require heavy seeds to reach the masses observed. This is consistent with our understanding of Eddington-limited accretion, which predicts growth timescales of light SMBH seeds ($100\,M_{\odot}$) up to $\sim 10^9$ to be approximately the age of the Universe at $z \sim 6$ (with $f_{\rm duty} \sim 1$) (K. Inayoshi et al. 2020). However, this is a simplistic model, and a more realistic approach would invoke long periods of sub-Eddington accretion followed by rapid bursts of super-Eddington accretion to better test if the masses observed can be reached via the growth of light BH seeds formed in the early Universe (M. Sanati et al. 2025).

6. Conclusion

In this work, we conduct SED fitting of 121 variable AGN identified in the HUDF by V. Cammelli et al. (2025) using 26 filters of PSF-matched photometry from HST and JWST. We designed a bespoke SED fitting code to test whether each source has an SED that is better modeled either by a pure SP using a delayed-τ SFH or if the fit is statistically improved by including an AGN template from M. J. Temple et al. (2021). We designed two conditions that would indicate if our SED fitting retrieved the AGN nature of the source, namely, the AIC condition, $\Delta{\rm AIC} \geqslant 6$, and the $\rm AGN_{frac}$ condition, where the AGN template contributes at least 20% to the total flux in at least one filter. In total, we identified 37 sources that meet the first condition, 26 sources that meet the latter, and 11 sources that meet both conditions. For the 26 sources meeting the $\rm AGN_{frac}$ condition, we use the model spectrum resulting from the MCMC SED fitting to calculate L_{5100}. We use this luminosity in conjunction with the scaling relation from S. Kaspi et al. (2000) to determine estimates for the BH masses of these objects. These mass estimates allow us to conclude the following:

1. Using the stellar masses from the SED fitting procedure, we plot our sources on the $M_{\rm BH}$–M_* plane and see that our sources become increasingly overmassive as a function of host redshift. This provides independent support for a systematic offset from the local relations as observed for other high-z BL-AGN detected with JWST. These overmassive BHs are possibly explained by either heavy seeding in the early Universe or episodes of super-Eddington accretion, especially for those sources in our sample with $M_{\rm BH} \sim M_*$.

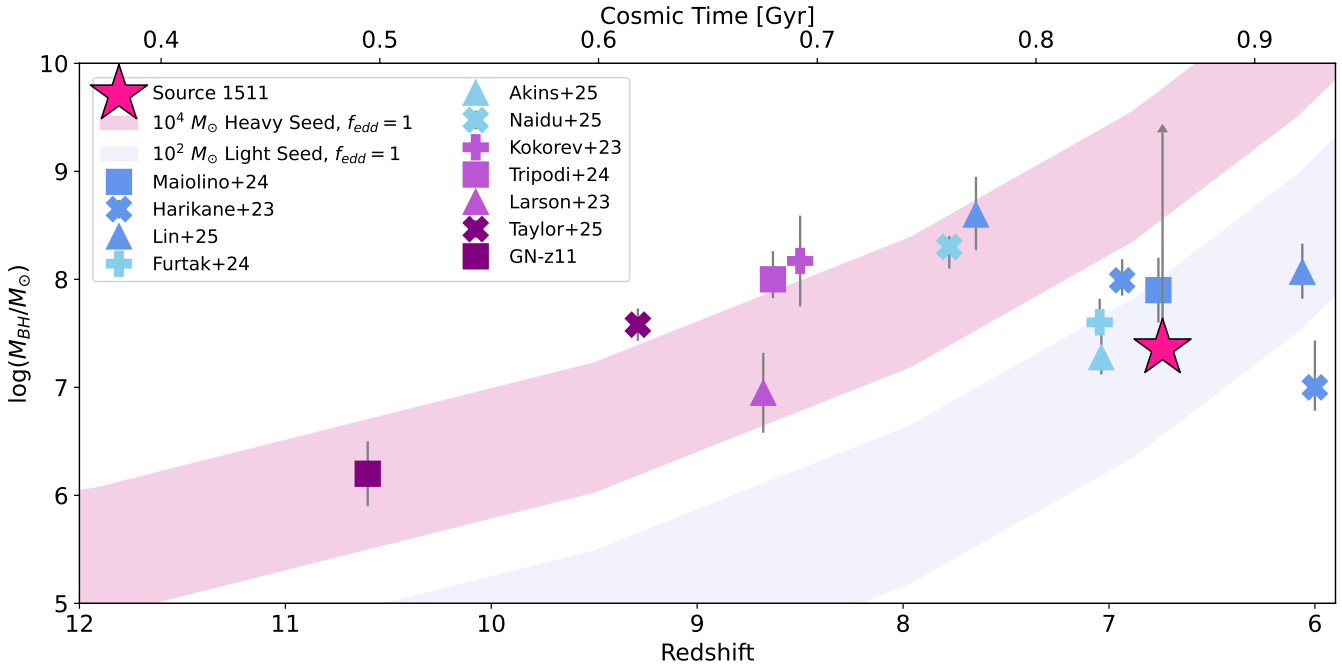

Figure 8. Adapted version of Figure 6 from A. J. Taylor et al. (2025) showing black hole mass as a function of redshift plotted for our highest-redshift variable source, 1511, marked here as the pink star. Spectroscopically confirmed BL-AGN from Y. Harikane et al. (2023), V. Kokorev et al. (2023), R. L. Larson et al. (2023), S. Tacchella et al. (2023), L. J. Furtak et al. (2024), R. Tripodi et al. (2025), R. Maiolino et al. (2024a, 2024b), H. B. Akins et al. (2025), X. Lin et al. (2026), R. P. Naidu et al. (2025), and A. J. Taylor et al. (2025) are shown by the filled markers. We note that GN-z11 is included in the analysis in R. Maiolino et al. (2024a); however, the parameters are determined in S. Tacchella et al. (2023) and R. Maiolino et al. (2024b). We overplot the growth of light and heavy seeds following a simple Eddington growth model as presented in A. J. Taylor et al. (2025). The bounds of the pink-shaded region correspond to the growth of massive seeds ($10^4 M_\odot$) formed at redshifts of 25 and 15, which then immediately begin to accrete mass at the Eddington limit. The bounds of the blue-shaded region show the mass evolution of light seeds ($10^2 M_\odot$) formed at redshifts of 30 and 15, which do not build up mass for the first 100 Myr, at which point they start accreting at the Eddington limit. The lower limit on the black hole mass for Source 1511 is consistent with sources at similar redshift from the literature and can be explained by both a heavy seeding scenario and our simple model for the Eddington growth of a light seed.

2. Our SED fitting results allow us to correct both our model stellar template and AGN template for reddening. We find that neglecting this correction can reduce the calculated BH mass by factors of up to $\simeq$10.
3. We compare the BH masses estimated for each source when photometry from the WFC3/IR epochs where the AGN is faint is used versus when the AGN is bright and find this can have considerable impact on the resulting BH mass by up to $\sim$3 dex where bright epochs yield higher $M_{\rm BH}$.
4. We identify two dwarf galaxies at $z < 1$ for which an AGN contribution to the SED is statistically preferred. The sources also exhibit BH masses that are overmassive with respect to the stellar mass of their host galaxies, which is consistent with observations of other IMBHs in dwarf galaxies (C. J. Burke et al. 2022; M. Mezcua et al. 2023; M. Siudek et al. 2023). Our dwarf galaxies also host BHs with masses that are systematically lower than those identified from spectroscopic features in A. E. Reines et al. (2013). This could indicate that variability offers a unique probe for identifying lower-mass BHs in dwarf galaxies, which is consistent with the results from E. Kimbro et al. (2025).
5. Finally, our highest-redshift variable for which we calculate a BH mass has an SED best explained by an $\rm AGN_{frac} \sim 1$. When compared to simple models for the Eddington growth of heavy seeds and light seeds as a function of redshift, the BH mass of 1511 is consistent with both seeding scenarios within errors. However, the value calculated as the lower limit for the BH mass can be explained by a light seed growing at the Eddington rate starting from 100 Myr after its formation.

Our work highlights the important role variability can play in identifying BHs and the effect this intrinsic phenomenon can have on the calculated mass of BHs. It also offers confirmation of observed trends in the $M_{\rm BH}$–M_* plane, which have been identified by JWST BL-AGN at high-z. Additionally, it does so by estimating BH masses using a method that does not require the measurement of broad-line properties and instead leverages the decomposition of the SEDs of our sources into separate AGN and stellar components.

Spectroscopic follow-up for the sample of 2.5σ variables presented in V. Cammelli et al. (2025) and studied here would allow us to better understand the intersection of different detection methods in identifying AGN. This work would be similar to the studies conducted by E. Pouliasis et al. (2019) and J. Lyu et al. (2022); however, spectra from JWST would allow us to probe the broad-line emission of AGN to much higher redshifts than was possible for the HUDF in these previous studies. This would be complimented by the relatively longer time baseline of our photometric variability study and the depth of the WFC3/IR images, which allow us to probe faint, low-mass AGN as well as the broad photometric coverage leveraged in this work. Studies of this nature are essential for determining how the properties of host galaxies and their SMBHs are linked and how they evolve through cosmic time.

Acknowledgments

We thank Pierluigi Monaco for useful discussions and invaluable contributions to the project and the anonymous referee for the constructive report that helped clarify our results and improve the content of this manuscript. A.R.Y. is funded by the Swedish National Space Agency, SNSA. M.J.H. is supported by the Swedish Research Council (Vetenskapsrådet) and is Fellow of the Knut & Alice Wallenberg Foundation. V.C. thanks the BlackHoleWeather project and PI Prof. Gaspari for salary support. The HST and JWST data presented in this article were obtained from the Mikulski Archive for Space Telescopes (MAST) at the Space Telescope Science Institute. The specific HST observations analyzed can be accessed via doi: 10.17909/7s5v-gz68, and the JWST observations can be accessed via JADES @MAST (M. Rieke et al. 2023a, doi: 10.17909/8tdj-8n28) and JEMS @MAST (C. Williams et al. 2023, doi: 10.17909/fsc4-dt61).

Facilities: HST (ACS/WFC, WFC3/UVIS, WFC3/IR), JWST (NIRCam, NIRISS).

Software: Astropy (Astropy Collaboration et al. 2013, 2018, 2022); DrizzlePac (STSCI Development Team 2012); SWarp (E. Bertin et al. 2002); PyPHER (A. Boucaud et al. 2016); ACSTOOLS (P. L. Lim et al. 2020); STPSF (M. D. Perrin et al. 2012); Source Extractor (E. Bertin & S. Arnouts 1996); SciPy (P. Virtanen et al. 2020); LMFIT (M. Newville et al. 2016); emcee (D. Foreman-Mackey et al. 2013); CIGALE (M. Boquien et al. 2019; I. E. López et al. 2024); BAGPIPES (A. C. Carnall et al. 2018); CLOUDY (G. J. Ferland et al. 2017).

Appendix A
Deriving Error Corrections for SExtractor Photometry

This appendix details the error correction applied to `Source Extractor` output photometry derived from the source injections introduced in Section 2. The F480M PSF was used as the injection PSF and renormalized to fluxes corresponding to an injection magnitude iteratively until 1000 sources had been injected at each magnitude in each filter image (however, only 10 sources were injected into an image at a time to avoid crowding). A segmentation map of the HUDF was used as a mask, and sources could only be injected into unmasked regions with a 50 pixel buffer to ensure the PSF wings were not overlapping with true sources. Sources were injected with AB magnitudes from 26 to 31.5 with $\delta_{\rm mag} = 0.5$ for $26 \leqslant {\rm mag} \leqslant 27$ and $\delta_{\rm mag} = 0.1$ for $27 < {\rm mag} \leqslant 31.5$. The exceptions were the UVIS filters for which $\delta_{\rm mag} = 0.1$ for the full magnitude range of $25 \leqslant {\rm mag} \leqslant 31.5$.

Once sources were injected into the image with a given magnitude, `Source Extractor` was used to determine the recovered magnitudes of each source. The injected sources and the recovered magnitudes were extracted from the `Source Extractor` catalogs using the known positions assigned to the injected sources and a tolerance of 1.5 pixels in x and y. For a given set of 1000 injected sources at a given magnitude, the retrieved magnitudes are plotted as a histogram. Histograms of the retrieved magnitudes for a subsample of injected magnitudes for the F140W image is shown in Figure 9. For each histogram, we calculate the standard deviation of the retrieved magnitudes to give the 1σ error for sources with a true magnitude corresponding to the injected magnitude. We then use these values to derive our `Source Extractor` error correction factor. The derivation of this correction factor is visualized in Figure 10, and we will refer to this figure as an example in the text that follows.

The standard deviations of each injected magnitude for a given filter image are then plotted, as represented by the orange points in Figure 10. To compare to the errors provided by `Source Extractor`, the photometry from the full catalog of sources in the HUDF is sorted into the same magnitude bins described above, and the mean error reported from the `Source Extractor` output is determined for each magnitude bin. These values correspond to the blue triangle data points in Figure 10. The offset between the orange and blue points then corresponds to the error correction, which must be applied to the photometric errors output from `Source Extractor`. To determine this offset, second-order polynomials are fit using `np.polyfit` to both the standard deviation in the retrieved magnitudes in all magnitude bins (the best-fit curve corresponding to the red line in Figure 10) as well as the mean error of the `Source Extractor` data (the best-fit curve corresponding to the navy line in Figure 10). These were fit from the brightest magnitude bin until the magnitude bin corresponding to the last magnitude bin before the retrieved fraction of the injected sources reached 90% (in Figure 10, this magnitude bin in marked by magenta outlines around the relevant data point and corresponds to $\mathrm{mag_{AB}} = 29.7$ for the F140W 2023 epoch image). We use this magnitude bin as the limiting magnitude for each filter image. We do not fit the polynomials beyond this limiting magnitude due to the fact that the number of retrieved sources is reduced such that the distribution of retrieved magnitudes suffers from low number statistics. These low numbers result in artificially reduced standard deviations represented by the inflection point in the orange points in Figure 10. The coefficients of these polynomials are determined and used to calculate the correction for any source with a reported `Source Extractor` magnitude (`MAG_SE`) and magnitude error (`MAGERR_SE`). For this, we calculate the value of the polynomial best fit to the injected source standard deviations (using the polynomial coefficients corresponding to the red curve in Figure 10) for the `Source Extractor` magnitude of a source (injected_poly(`MAG_SE`)) as well as the value of the polynomial best fit to the mean errors from the HUDF catalog (using the polynomial coefficients corresponding to the navy curve in Figure 10) for the same source (data_poly (`MAG_SE`)). The correction factor (err_corr) then becomes

$$\mathrm{err\_corr} = \frac{\mathrm{injected\_poly(MAG\_SE)}}{\mathrm{data\_poly(MAG\_SE)}}. \tag{A1}$$

This allows for the calculation of the corrected error as `MAGERR_corr` = `MAGERR_SE` +err_corr. This correction must be applied to each source for the photometric measurement in each filter using the relevant polynomial coefficients determined from source injections in each filter.

We also note that Figure 9 demonstrates that our correction factor additionally contains an aperture correction. In these histograms, when the injected magnitude is brighter than the limiting magnitude, the mean retrieved magnitude is always fainter than the injected magnitude, even for bright source injections. This difference between the mean retrieved magnitude and the injected magnitude captures the aperture correction since a reduced fraction of the flux is captured for sources that are not pointlike when aperture photometry is used.

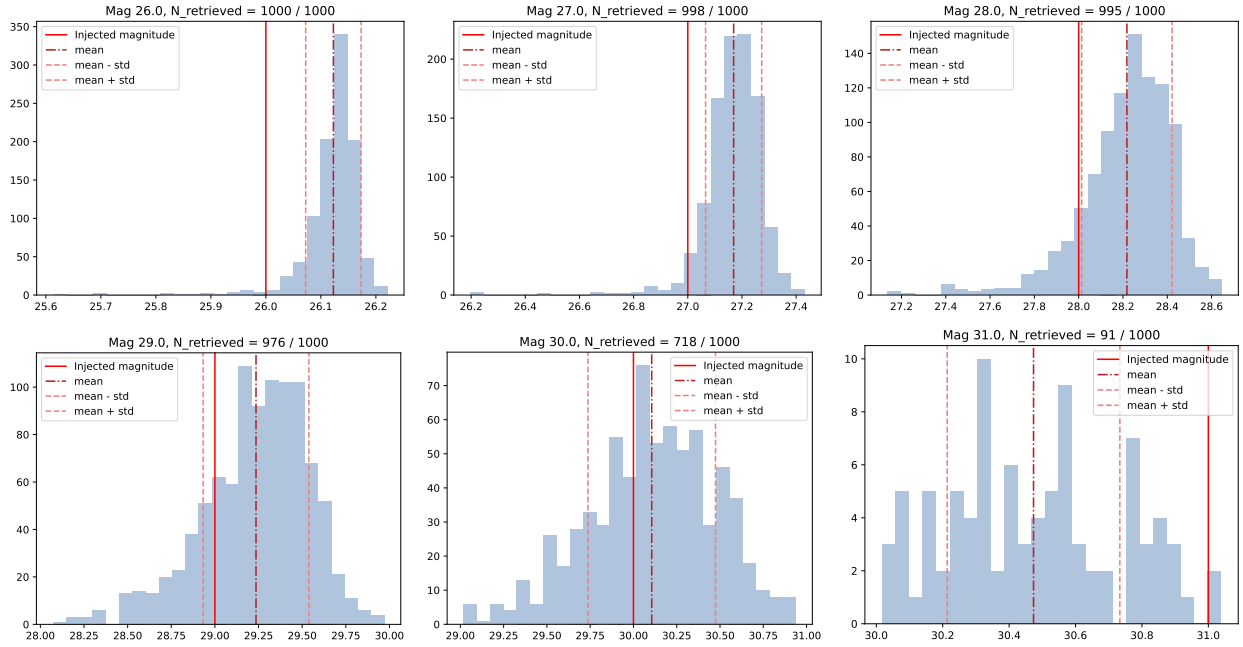

Figure 9. Histograms showing the magnitudes returned from `Source Extractor` for each retrieved source injected with a given magnitude, which is recorded in the subtitle of each plot. The red solid line shows the injected magnitude, the burgundy-dashed–dotted line indicates the mean of the retrieved magnitudes, and the pink-dashed lines show the 1σ values of the retrieved magnitude distribution. This represents a subset of the injected magnitudes for the F140W filter. Here, we can also see that when the injected magnitude is brighter than the limiting magnitude the mean of the retrieved magnitudes is always fainter than the injected magnitude, even for bright source injections. This difference between the mean of the retrieved magnitude and the injected magnitude captures the aperture correction since a reduced fraction of the flux is captured for sources that are not pointlike when aperture photometry is used.

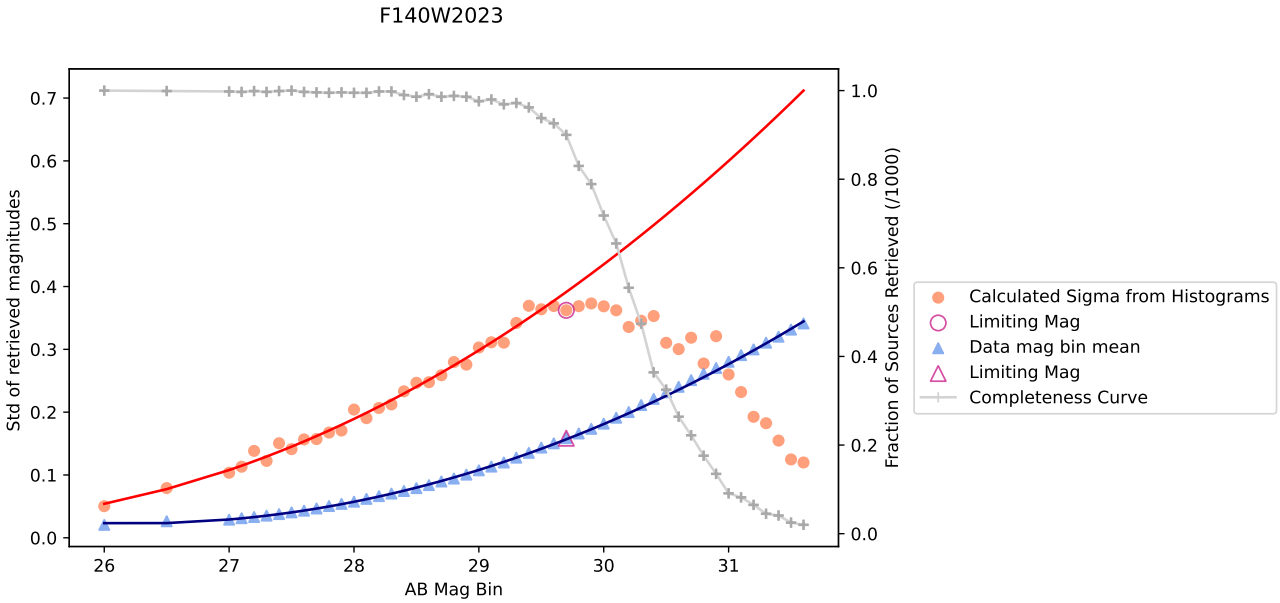

Figure 10. Demonstration of how the `Source Extractor` error correction factor is determined for each filter, here shown for the F140W filter. The gray curve represents the number of sources retrieved for each injected magnitude; this is our completeness curve. When this curve drops below the 90% completeness limit, we consider the previous injected magnitude our limiting magnitude. This limiting magnitude is represented by the magenta-outlined points. The standard deviation of the retrieved magnitudes for each injected magnitude are shown by the orange circular points. The blue triangles represent the mean `Source Extractor` error for sources in our photometric catalog with `Source Extractor` magnitudes in each magnitude bin. The best-fit second-order polynomial for the orange points is shown as the red curve, and the best-fit curve for the blue points is given by the navy curve. The difference between the polynomials represented by the red and blue curves are used to calculate the error correction factor for each source in our catalog. See text for details.

Appendix B
Artificial Star Injections: Testing the Surplus of Detected Variables Getting Brighter between Epochs

We noticed that a surplus of variable sources in the HUDF appeared to get brighter between epochs when compared to the number that appear to get fainter. To test whether there was a bias in our detection methods, a series of tests were executed by inserting artificial sources into the difference images. This was done by iteratively inserting 10 artificial stars into the first epoch in the time series, subtracting the second epoch, and performing photometry with `Source Extractor` on the

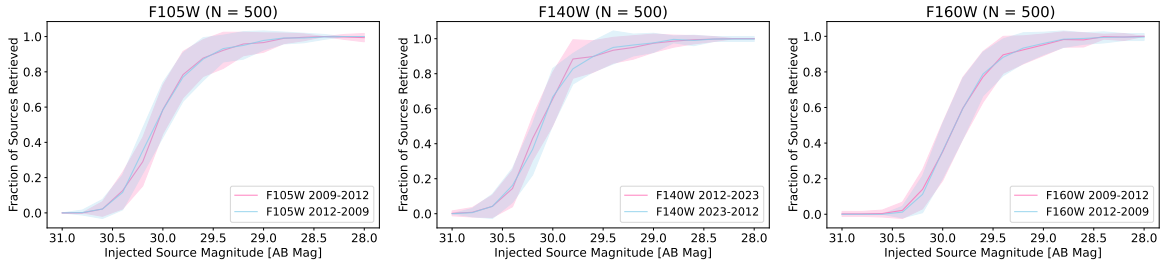

Figure 11. Results from the artificial stars tests seeking to determine if there is a detection bias for variables that get brighter between epochs. Plots show the fraction of injected sources retrieved from the total sample in each magnitude bin ($N = 500$) for the F105W, F140W, and F160W filters. The different curves show the different results when difference images are generated both by inserting the artificial sources into the early epoch and performing image subtraction in pink and by inserting the sources into the late epoch and performing image subtraction in blue. Within errors, the two scenarios are consistent, meaning no significant bias exists in our photometry to select either preferentially dimming nor brightening sources.

resulting difference image to determine the fraction of inserted sources retrieved at a given magnitude. 50 images containing 10 artificial sources were generated in each magnitude bin. For each filter, this is performed twice such that the fraction of sources retrieved when the difference image is created by inserting artificial stars into the first epoch can be tested against the number of sources retrieved when the difference image is instead generated by inserting stars into the second epoch before subtraction. Stars were generated at a given magnitude between 29.0 and 31.0 with a step size of 0.2 mag using the `make_gaussian_sources_image` from the *Photutils* affiliated package of *Astropy*. These sources are assigned a random position in the masked field, which excludes areas of the image that are less deep because of either pointing offsets (at the edge of the image) or persistence (and therefore have fewer images contributing to the total stack in the respective area of the image). `Source Extractor` is then used to perform source detection and photometry on the resulting difference image. The recovered source positions are then compared to the input positions of the artificial stars with a tolerance of 1.5 pixels in x and y as well as the recovered magnitude of the source, which must be with 0.5 mag of the input magnitude. The fraction of retrieved sources from these tests for the F105W, F140W, and F160W filters is presented in Figure 11. Within errors, the results show that the artificial star tests are not affected by which epoch the artificial stars are inserted into. Physically, this would mean that our results are not biased toward either variable objects, which get brighter, nor variables, which get fainter.

Appendix C
Comparison of Results from the "Best-fit" Model versus the "Most Probable" Model

In Section 3, we discuss the choice to define both a best-fit model and a most probable model due to considerations regarding the differences between model selection and parameter estimation. In this appendix, we further motivate this choice by first demonstrating the complex nature of our posterior distributions and comparing the final BH and stellar masses that result from both the best-fit and most probable models. First, Figure 12 shows an example corner plot for source 3902. D. W. Hogg & D. Foreman-Mackey (2018) emphasize that the best-fitting model may not correspond to the most probable model when the posterior distribution is complex and, specifically, when they are wide. As such, Figure 12 demonstrates that the final posteriors meet these conditions. This justifies our decision to use the results from the minimizer to determine whether the fit is improved by incorporating an AGN template (i.e., identifying the "best" model) while using the MCMC results for our parameter estimation and using the confidence intervals to assign errors to our parameters. In some cases, our fitter actually identified best-fit model parameters that lay outside of the MCMC confidence intervals, further emphasizing the need to use this dual approach. Source 3902 is such a source, and the differences in the resulting parameters are shown in Figure 12 via the column text stating the MCMC mean values for each parameter in contrast to the plotted blue data points on each contour plot indicating the best-fit result from the minimizer. In this case, most of the blue points lie at the edges of the contours. In contrast, Figure 13 shows the corner plot for source 2460; the mean MCMC results agree well with the minimizer best-fit values, meaning the blue points are within the 16th and 84th percentiles for each distribution.

Second, we identified sources that had best-fit model parameters that did not correspond to values within the range between the 16th and 84th percentiles reported from the MCMC sampler that meet our $\mathrm{AGN}_{\mathrm{frac}}$ criterion. For these sources, we iteratively compute $M_{\mathrm{BH,int}}$ and M_* using both the best-fit results and the most probable results. As illustrated in Figure 14, with the exception of a single outlier, the values calculated from both fits agree well. As such, we conclude that this dual approach does not strongly affect the final masses calculated from the model parameters and only acts as a means to more strongly define the "best-fit" model when determining the ability of the SED fitter to retrieve the AGN nature of our sources.

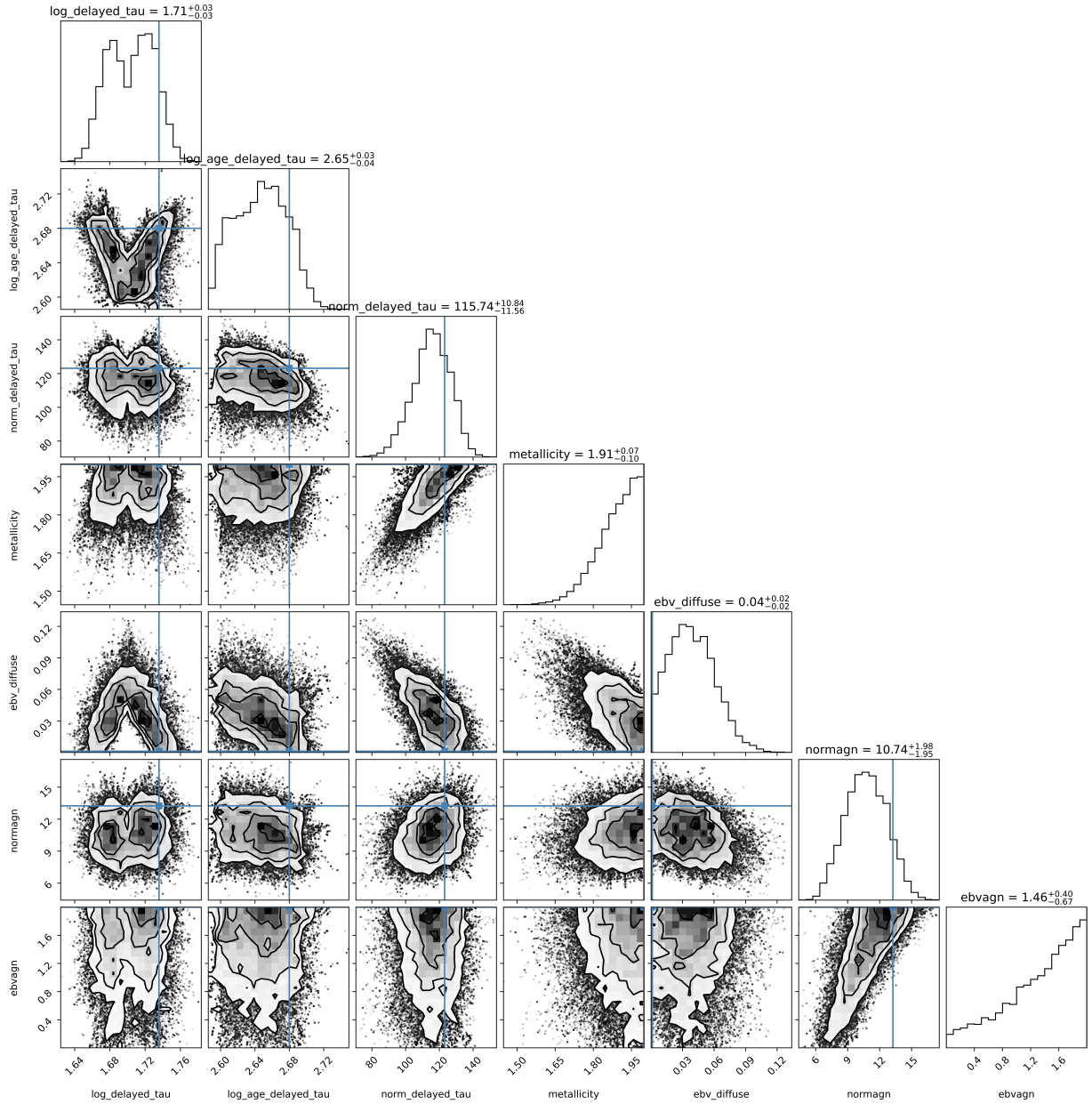

Figure 12. Corner plot from the MCMC sampler for source 3902 where the values listed in the column titles correspond to the MCMC medians while the blue markers indicate the best-fit results from the minimizer. This source has best-fit values that lie outside the 16th and 84th percentiles determined from the MCMC sampler for several parameters (including `log_delayed_tau`, `log_age_delayed_tau`, `metallicity`, `ebv_diffuse`, `norm_agn`, and `ebv_agn`). This illustrates the wide posteriors, which mean that the maximum a posteriori estimate given by the least-squares fitter may give a better estimate of the best-fit model instead of the MCMC median (D. W. Hogg & D. Foreman-Mackey 2018).

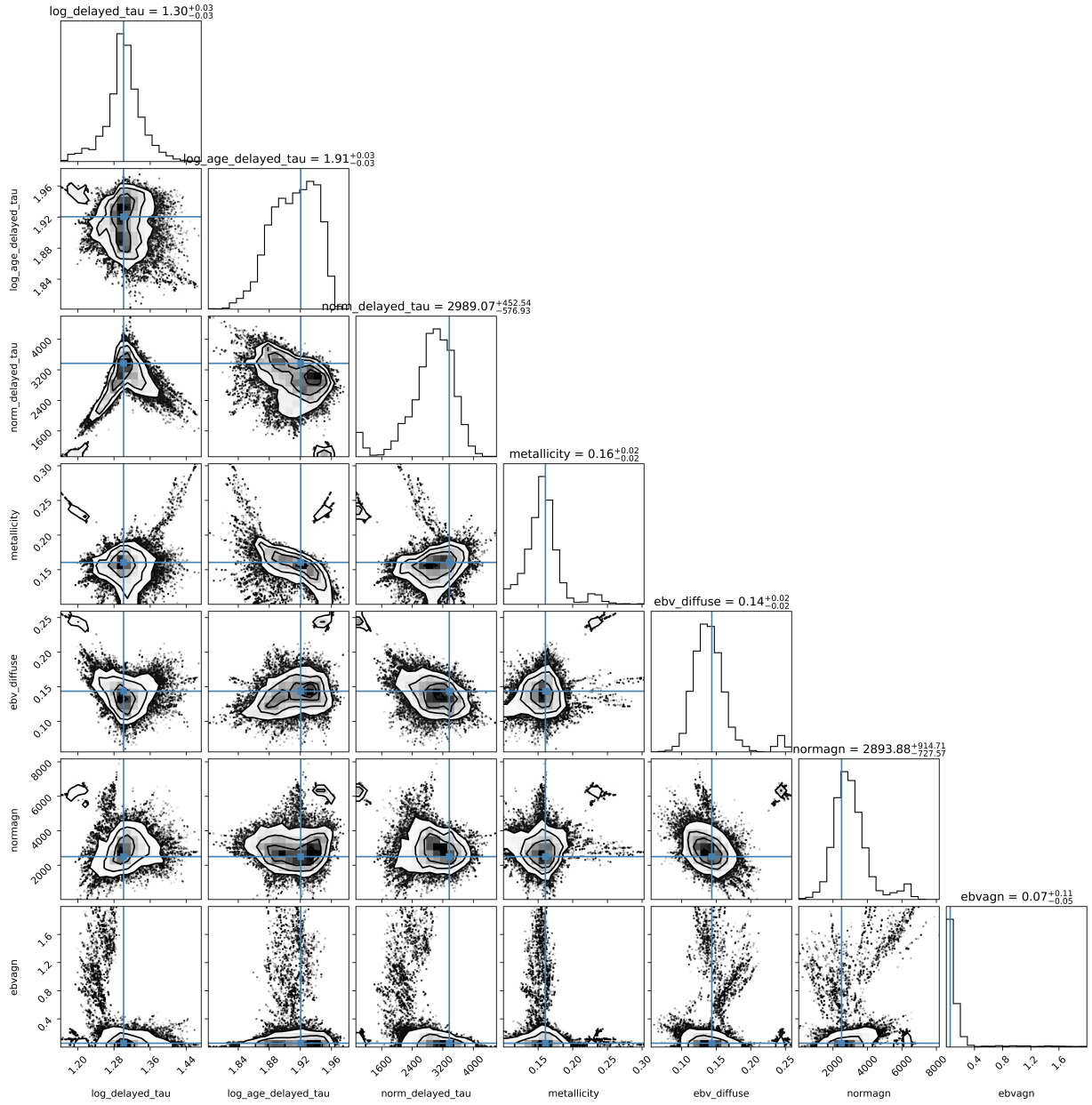

Figure 13. Same as Figure 12 for source 2460. This source is shown for completeness and illustrates the case where the MCMC median values agree with the results from the minimizer as the blue points marking the best-fit results fall within the 16th and 84th percentiles for each parameter.

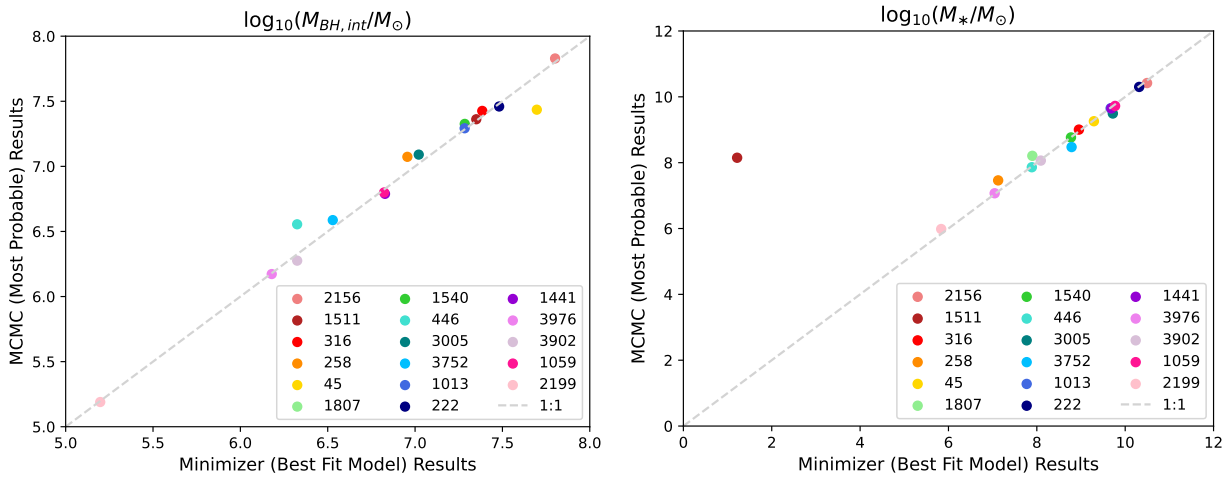

Figure 14. Comparison between the derived values for $\log_{10}(M_{\rm BH,int}/M_\odot)$ (left) and $\log_{10}(M_*/M_\odot)$ (right) determined from the best-fit model (maximum a posteriori from the minimizer) versus the most probable model (MCMC sampler median) parameters. With the exception of the stellar masses for source 1511 (for which we only estimate lower limits), these values are all in relatively good agreement. This highlights that the final parameters are not strongly affected by the choice of either the most probable or the best-fit model.

ORCID iDs

Alice R. Young https://orcid.org/0000-0001-9136-3701
Matthew J. Hayes https://orcid.org/0000-0001-8587-218X
Alberto Saldana-Lopez https://orcid.org/0000-0001-8419-3062
Axel Runnholm https://orcid.org/0000-0002-1025-7569
Vieri Cammelli https://orcid.org/0000-0002-2070-9047
Jonathan C. Tan https://orcid.org/0000-0002-3389-9142
Richard S. Ellis https://orcid.org/0000-0001-7782-7071
Benjamin W. Keller https://orcid.org/0000-0002-9642-7193
Jens Melinder https://orcid.org/0000-0003-0470-8754
Jasbir Singh https://orcid.org/0000-0002-6260-1165

References

Abuter, R., Allouche, F., Amorim, A., et al. 2024, Natur, 627, 281
Akins, H. B., Casey, C. M., Berg, D. A., et al. 2025, ApJL, 980, L29
Akins, H. B., Casey, C. M., Lambrides, E., et al. 2025, ApJ, 991, 37
Arévalo, P., Churazov, E., Lira, P., et al. 2024, A&A, 684, A133
Astropy Collaboration, Price-Whelan, A. M., Lim, P. L., et al. 2022, ApJ, 935, 167
Astropy Collaboration, Price-Whelan, A. M., Sipőcz, B. M., et al. 2018, AJAJ, 156, 123
Astropy Collaboration, Robitaille, T. P., Tollerud, E. J., et al. 2013, A&A, 558, A33
Bacon, R., Brinchmann, J., Conseil, S., et al. 2023, A&A, 670, A4
Bañados, E., Venemans, B. P., Mazzucchelli, C., et al. 2017, Natur, 553, 473
Banik, N., Tan, J. C., & Monaco, P. 2019, MNRAS, 483, 3592
Barro, G., Perez-Gonzalez, P. G., Kocevski, D. D., et al. 2024, ApJ, 963, 128
Begelman, M. C., Volonteri, M., & Rees, M. J. 2006, MNRAS, 370, 289
Bennett, J. S., Sijacki, D., Costa, T., Laporte, N., & Witten, C. 2024, MNRAS, 527, 1033
Bertin, E., & Arnouts, S. 1996, A&AS, 117, 393
Bertin, E., Mellier, Y., Radovich, M., et al. 2002, ASPC, 281, 228
Boquien, M., Burgarella, D., Roehlly, Y., et al. 2019, A&A, 622, A103
Boucaud, A., Dole, H., Abergel, A., Ayasso, H., & Orieux, F. 2016, EAS Publications Series, 78, 275
Brammer, G. 2016, Instrument Science Report WFC3 2016-16,
Bressan, A., Marigo, P., Girardi, L., et al. 2012, MNRAS, 427, 127
Bromm, V., & Loeb, A. 2003, ApJ, 596, 34
Bruzual, G., & Charlot, S. 2003, MNRAS, 344, 1000
Bunker, A. J., Cameron, A. J., Curtis-Lake, E., et al. 2024, A&A, 690, A288
Burke, C. J., Liu, X., Shen, Y., et al. 2022, MNRAS, 516, 2736
Burnham, K. P., & Anderson, D. R. 2002, Model Selection and Multimodel Inference: A Practical Information-Theoretic Approach (Springer)
Calzetti, D., Armus, L., Bohlin, R. C., et al. 2000, ApJ, 533, 682
Cammelli, V., Monaco, P., Tan, J. C., et al. 2025, MNRAS, 536, 851
Cammelli, V., Tan, J. C., Young, A. R., et al. 2025, ApJ, 991, 141
Carnall, A. C., McLure, R. J., Dunlop, J. S., & Davé, R. 2018, MNRAS, 480, 4379
Chon, S., Hirano, S., Hosokawa, T., & Yoshida, N. 2016, ApJ, 832, 134
Cohen, S. H., Ryan, R. E., Jr., Straughn, A. N., et al. 2006, ApJ, 639, 731
Dalla Bontà, E., Peterson, B. M., Grier, C. J., et al. 2025, A&A, 696, A48
DeCoursey, C., Egami, E., Pierel, J. D. R., et al. 2025, ApJ, 979, 250
Eisenstein, D. J., Johnson, B. D., Robertson, B., et al. 2025, ApJS, 281, 50
Falcón-Barroso, J., Sánchez-Blázquez, P., Vazdekis, A., et al. 2011, A&A, 532, A95
Fan, X., Banados, E., & Simcoe, R. A. 2023, ARA&A, 61, 373
Fan, X., Narayanan, V. K., Lupton, R. H., et al. 2001, AJ, 122, 2833
Fan, X., Strauss, M. A., Schneider, D. P., et al. 1999, AJ, 118, 1
Ferland, G. J., Chatzikos, M., Guzmán, F., et al. 2017, RMxAA, 53, 385
Fonseca Alvarez, G., Trump, J. R., Homayouni, Y., et al. 2020, ApJ, 899, 73
Foreman-Mackey, D., Hogg, D. W., Lang, D., & Goodman, J. 2013, PASP, 125, 306
Freitag, M., Rasio, F. A., & Baumgardt, H. 2006, MNRAS, 368, 121
Furtak, L. J., Labbé, I., Zitrin, A., et al. 2024, Natur, 628, 57
Furtak, L. J., Zitrin, A., Plat, A., et al. 2023, ApJ, 952, 142
Granato, G. L., De Zotti, G., Silva, L., Bressan, A., & Danese, L. 2004, ApJ, 600, 580
Gravity Collaboration, Sturm, E., Dexter, J., et al. 2018, Natur, 563, 657
Greene, J. E., & Ho, L. C. 2005, ApJ, 630, 122
Greene, J. E., Labbe, I., Goulding, A. D., et al. 2024, ApJ, 964, 39
Greene, J. E., Strader, J., & Ho, L. C. 2020, ARA&A, 58, 257
Haehnelt, M. G., & Rees, M. J. 1993, MNRAS, 263, 168
Haiman, Z., & Loeb, A. 2001, ApJ, 552, 459
Harikane, Y., Zhang, Y., Nakajima, K., et al. 2023, ApJ, 959, 39
Hayes, M. J., Tan, J. C., Ellis, R. S., et al. 2024, ApJL, 971, L16
Ho, L. C., & Kim, M. 2016, ApJ, 821, 48
Hogg, D. W., & Foreman-Mackey, D. 2018, ApJS, 236, 11
Hook, I. M., & McMahon, R. G. 1998, MNRAS, 294, L7
Hopkins, P. F., Hernquist, L., Cox, T. J., et al. 2006, ApJS, 163, 1
Illingworth, G. D., Magee, D., Oesch, P. A., et al. 2013, ApJS, 209, 6
Inayoshi, K., Visbal, E., & Haiman, Z. 2020, ARA&A, 58, 27
Johnson, J. L., & Bromm, V. 2007, MNRAS, 374, 1557
Kaspi, S., Smith, P. S., Netzer, H., et al. 2000, ApJ, 533, 631
Kimbro, E., Baldassare, V., Worthey, G., Geha, M., & Greene, J. 2025, ApJ, 980, 215
Kocevski, D. D., Onoue, M., Inayoshi, K., et al. 2023, ApJL, 954, L4
Koekemoer, A. M., Ellis, R. S., McLure, R. J., et al. 2013, ApJS, 209, 3
Kokorev, V., Caputi, K. I., Greene, J. E., et al. 2024, ApJ, 968, 38
Kokorev, V., Fujimoto, S., Labbe, I., et al. 2023, ApJL, 957, L7
Korista, K. T., & Goad, M. R. 2004, ApJ, 606, 749
Kormendy, J., & Ho, L. C. 2013, ARA&A, 51, 511
Koudmani, S., Sijacki, D., & Smith, M. C. 2022, MNRAS, 516, 2112
Kroupa, P. 2001, MNRAS, 322, 231

Labbe, I., Greene, J. E., Matthee, J., et al. 2024, arXiv: 2412.04557
Larson, R. L., Finkelstein, S. L., Kocevski, D. D., et al. 2023, ApJL, 953, L29
Leung, G. C. K., Finkelstein, S. L., Pérez-González, P. G., et al. 2025, ApJ, 992, 26
Li, Y., Hernquist, L., Robertson, B., et al. 2007, ApJ, 665, 187
Lim, P. L., Davis, M., Hack, W., et al. 2020, ACStools: Python tools for Hubble Space Telescope Advanced Camera for Surveys data, Astrophysics Source Code Library, ascl:2011.024
Lin, X., Fan, X., Wang, F., et al. 2026, ApJ, 996, 93
López, I. E., Yang, G., Mountrichas, G., et al. 2024, A&A, 692, A209
Lyu, J., Alberts, S., Rieke, G. H., & Rujopakarn, W. 2022, ApJ, 941, 191
Ma, Y., Greene, J. E., Setton, D. J., et al. 2025, ApJ, 981, 191
Madau, P. 1995, ApJ, 441, 18
Madau, P., & Rees, M. J. 2001, ApJL, 551, L27
Maiolino, R., Scholtz, J., Curtis-Lake, E., et al. 2024a, A&A, 691, A145
Maiolino, R., Scholtz, J., Witstok, J., et al. 2024b, Natur, 627, 59
Marigo, P., Bressan, A., Nanni, A., Girardi, L., & Pumo, M. L. 2013, MNRAS, 434, 488
Marshall, A., Auger-Williams, M. W., Banerji, M., Maiolino, R., & Bowler, R. 2022, MNRAS, 515, 5617
Matsuoka, Y., Onoue, M., Kashikawa, N., et al. 2019, ApJL, 872, L2
Matsuoka, Y., Strauss, M. A., Kashikawa, N., et al. 2018, ApJ, 869, 150
Matthee, J., Naidu, R. P., Brammer, G., et al. 2024, ApJ, 963, 129
McCaffrey, J., Regan, J., Smith, B., et al. 2025, OJAp, 8, 11
McKee, C. F., & Tan, J. C. 2008, ApJ, 681, 771
Mezcua, M., Siudek, M., Suh, H., et al. 2023, ApJL, 943, L5
Mortlock, D. J., Warren, S. J., Venemans, B. P., et al. 2011, Natur, 474, 616
Naidu, R. P., Matthee, J., Katz, H., et al. 2025, arXiv: 2503.16596
Newville, M., Stensitzki, T., Allen, D. B., et al. 2016, Lmfit: Non-Linear Least-Square Minimization and Curve-Fitting for Python, Astrophysics Source Code, ascl:1606.014
O'Brien, R., Jansen, R. A., Grogin, N. A., et al. 2024, ApJS, 272, 19
Oke, J. B., & Gunn, J. E. 1983, ApJ, 266, 713
Perrin, M. D., Soummer, R., Elliott, E. M., Lallo, M. D., & Sivaramakrishnan, A. 2012, SPIE, 8442, 84423D
Pirzkal, N., Rothberg, B., Papovich, C., et al. 2024, ApJ, 969, 90
Pouliasis, E., Georgantopoulos, I., Bonanos, A. Z., et al. 2019, MNRAS, 487, 4285
Prevot, M. L., Lequeux, J., Maurice, E., Prevot, L., & Rocca-Volmerange, B. 1984, A&A, 132, 389
Rafelski, M., Teplitz, H. I., Gardner, J. P., et al. 2015, AJ, 150, 31
Rees, M. J. 1978, IAUS, 77, 237
Regan, J., & Volonteri, M. 2024, OJAp, 7, 72
Reines, A. E., Greene, J. E., & Geha, M. 2013, ApJ, 775, 116
Reines, A. E., & Volonteri, M. 2015, ApJ, 813, 82
Rieke, M., Robertson, B., Tacchella, S., et al. 2023a, Data from the JWST Advanced Deep Extragalactic Survey (JADES), STScI/MAST, doi:10.17909/8TDJ-8N28
Rieke, M. J., Robertson, B., Tacchella, S., et al. 2023b, ApJS, 269, 16
Robitaille, T., Deil, C., & Ginsburg, A. 2020, reproject: Python-based astronomical image reprojection, Astrophysics Source Code Library, ascl:2011.023
Sanati, M., Devriendt, J., Martin-Alvarez, S., Slyz, A., & Tan, J. C. 2025, MNRAS, 544, 4317
Schneider, D. P., Fan, X., Strauss, M. A., et al. 2000, AJ, 120, 2183
Schneider, D. P., Schmidt, M., Gunn, J. E., et al. 1994, AJ, 107, 880
Schneider, D. P., Schmidt, M., Gunn, J. E., et al. 2023, MNRAS, 521, 3972
Setton, D. J., Greene, J. E., de Graaff, A., et al. 2025, ApJ, 995, 118
Sijacki, D., Springel, V., & Haehnelt, M. G. 2009, MNRAS, 400, 100
Singh, J., Monaco, P., & Tan, J. C. 2023, MNRAS, 525, 969
Siudek, M., Mezcua, M., & Krywult, J. 2023, MNRAS, 518, 724
STSCI Development Team 2012, DrizzlePac: HST image software, Astrophysics Source Code Library, ascl:1212.011
Tacchella, S., Eisenstein, D. J., Hainline, K., et al. 2023, ApJ, 952, 74
Taylor, A. J., Kokorev, V., Kocevski, D. D., et al. 2025, ApJL, 989, L7
Temple, M. J., Hewett, P. C., & Banerji, M. 2021, MNRAS, 508, 737
Teplitz, H. I., Rafelski, M., Kurczynski, P., et al. 2013, AJ, 146, 159
Trinca, A., Schneider, R., Valiante, R., et al. 2022, MNRAS, 511, 616
Tripodi, R., Martis, N., Markov, V., et al. 2025, NatCo, 16, 9830
Übler, H., Maiolino, R., Curtis-Lake, E., et al. 2023, A&A, 677, A145
Valiante, R., Schneider, R., Volonteri, M., & Omukai, K. 2016, MNRAS, 457, 3356
Virtanen, P., Gommers, R., Oliphant, T. E., et al. 2020, NatMe, 17, 261
Volonteri, M. 2010, A&ARv, 18, 279
Volonteri, M., Haardt, F., & Madau, P. 2003, ApJ, 582, 559
Volonteri, M., Habouzit, M., & Colpi, M. 2023, MNRAS, 521, 241
Wang, B., de Graaff, A., Davies, R. L., et al. 2025, ApJ, 984, 121
Wang, F., Yang, J., Fan, X., et al. 2018, ApJL, 869, L9
Warren, S. J., Hewett, P. C., Irwin, M. J., McMahon, R. G., & Bridgeland, M. T. 1987, Natur, 325, 131
Wasleske, E. J., & Baldassare, V. F. 2023, AJ, 166, 64
Weaver, J. R., Cutler, S. E., Pan, R., et al. 2024, ApJS, 270, 7
Wiener, N. 1949, Extrapolation, Interpolation, and Smoothing of Stationary Time Series: With Engineering Applications (The MIT Press)
Williams, C., Tacchella, S., Maseda, M., et al. 2023, Data from the JWST Extragalactic Medium-band Survey (JEMS), STScI/MAST, doi:10.17909/FSC4-DT61
Williams, C. C., Tacchella, S., Maseda, M. V., et al. 2023, ApJS, 268, 64
Wise, J. H., Regan, J. A., O'Shea, B. W., et al. 2019, Natur, 566, 85
Yang, J., Wang, F., Fan, X., et al. 2019, AJ, 157, 236
Yang, J., Wang, F., Fan, X., et al. 2020, ApJL, 897, L14
Yoshida, N. 2006, NewAR, 50, 19
Yu, W., Richards, G. T., Vogeley, M. S., Moreno, J., & Graham, M. J. 2022, ApJ, 936, 132
Zaw, I., Rosenthal, M. J., Katkov, I. Y., et al. 2020, ApJ, 897, 111
Zhang, J., Egami, E., Sun, F., et al. 2025, Abundant Population of Broad Hα Emitters in the GOODS-N Field Revealed by CONGRESS, FRESCO, and JADES, Astrophysics Source Code Library, ascl:2505.02895